ELSEVIER

Journal of Contaminant Hydrology 38 (1999) 107–156

JOURNAL OF
Contaminant
Hydrology

Constraints on the hydrology of the unsaturated zone at Yucca Mountain, NV from three-dimensional models of chloride and strontium geochemistry

Eric L. Sonnenthal *, Gudmundur S. Bodvarsson

Earth Sciences Division, Lawrence Berkeley National Laboratory, One Cyclotron Road, MS90-1116, Berkeley, CA 94720, USA

Accepted 18 December 1998

Abstract

Three-dimensional (3-D) simulations of the spatial and temporal variations in chloride and strontium concentrations in porewaters were performed to constrain infiltration rates, flow paths, and mixing processes in the unsaturated zone (UZ) at Yucca Mountain, NV. Chloride concentrations in infiltrating water were calculated from aerial distributions of precipitation and infiltration rates for the current climatic conditions and for the last glacial maximum, combined with effective chloride concentrations in precipitation. Modeled concentrations are roughly similar to measured porewater chloride concentrations from the Paintbrush nonwelded tuffs in the Exploratory Studies Facility (ESF) tunnel and in boreholes suggesting that the mean infiltration rate over the site is unlikely to be higher than the calculated mean infiltration rate for the modern climate (~ 5 mm/year; [Flint, A.L., Hevesi, J.A., Flint, L.E., 1996. Conceptual and Numerical Model of Infiltration for the Yucca Mountain Area, Nevada. Milestone 3GU1623M. U.S. Geol. Surv. Water Res. Invest. Rep. U.S. Geological Survey, Denver, CO]). Porewaters from the late Pleistocene (> 10 ka) could be present in the Paintbrush bedded tuffs and in the underlying Topopah Spring welded tuffs (TSw), predominately under regions of thick alluvium having little infiltration. However, porewaters at the potential repository level may have a higher proportion of Holocene recharge due to the higher calculated infiltration rate in this region. Dual-permeability simulations show that in low infiltration regions chemical disequilibrium can exist between fracture and matrix porewaters, as a result of the climate change 10,000 years ago. Below the potential repository level, simulations show significant mixing due to lateral flow on top of the low permeability basal

* Corresponding author. Fax: +1-510-486-6115; e-mail: elsonnenthal@lbl.gov

0169-7722/99/$ - see front matter
PII: S0169-7722(99)00013-3

vitrophyre in the Topopah Spring unit and on zeolitized tuffs in the Calico Hills unit. Perched water chloride concentrations are closely matched using the calculated conditions for the last glacial maximum climate, with some component of Holocene recharge. Measured strontium concentrations in the UZ and in the perched water bodies can be roughly matched by assuming conservative behavior in nonzeolitic units and strong ion exchange in zeolitic units, and indicate that the perched water bodies are poorly mixed. Differences in the Cl contents of samples having a bomb-pulse Cl-36 signature and those with a modern ratio indicate that waters of intermediate $^{36}Cl/Cl$ ratios may be mixtures, that without other isotopic data could be inferred as either Pleistocene or Holocene age waters.

Keywords: Chloride; Strontium; Unsaturated zone; Yucca Mountain; Modeling

1. Introduction

Yucca Mountain, NV resides within a semiarid region of the southwestern United States, and is a potential site for the U.S. Department of Energy high level nuclear waste repository. It has been the subject of intensive geologic, hydrologic, and more recently, subsurface engineering studies (see other papers, this issue). A map of the region enclosing the potential repository is shown in Fig. 1, including the surface projection of the 8-km-long ESF tunnel, locations of deep boreholes, and the outline of the Lawrence Berkeley National Laboratory 3-D unsaturated zone (UZ) site-scale model SSM. The purpose of this work is to use models for the geochemical behavior of Cl and Sr to bound the infiltration rate and flow pathways, assess the model for the spatial distribution of infiltration (Flint et al., 1996), and evaluate conceptual models for the evolution of the UZ hydrologic system.

From a hydrological perspective, several issues concern the UZ that are important to assessing the performance of the repository. These include the percolation flux at the repository and possible seepage into the drifts, the flow paths below the repository and radionuclide retardation and transport times to the saturated zone (SZ). The percolation flux at the repository strongly depends on the magnitude and spatial distribution of surface infiltration over time. Much work has been done to calculate the infiltration flux based on models of evapotranspiration (Hevesi et al., 1992; Flint and Flint, 1994; Flint et al., 1996). Based mainly on the latter work, a recent analysis by an independent scientific (Geomatrix Consultants, 1997) concluded that the present mean infiltration could vary from less than 1 mm/year to several tens of millimeters per year.

In addition to the uncertainty in the present day infiltration flux, there is also uncertainty in the possible effect of climate change on infiltration. Variations in climate over the past 100,000 years or so have been used to estimate the possible range in infiltration rates over the next 10,000 years (J. Hevesi, personal communication). The

Fig. 1. Area map of region enclosing Yucca Mountain. Shown are traces of major faults, deep borehole locations, the outline of the potential repository, the position of the Exploratory Studies Facility (ESF) tunnel, and the outline of the three-dimensional (3-D) Site-Scale Model (SSM) boundary. Regions in white are the more prominent valleys ('washes'). Map provided by Jennifer Hinds (Lawrence Berkeley National Laboratory).

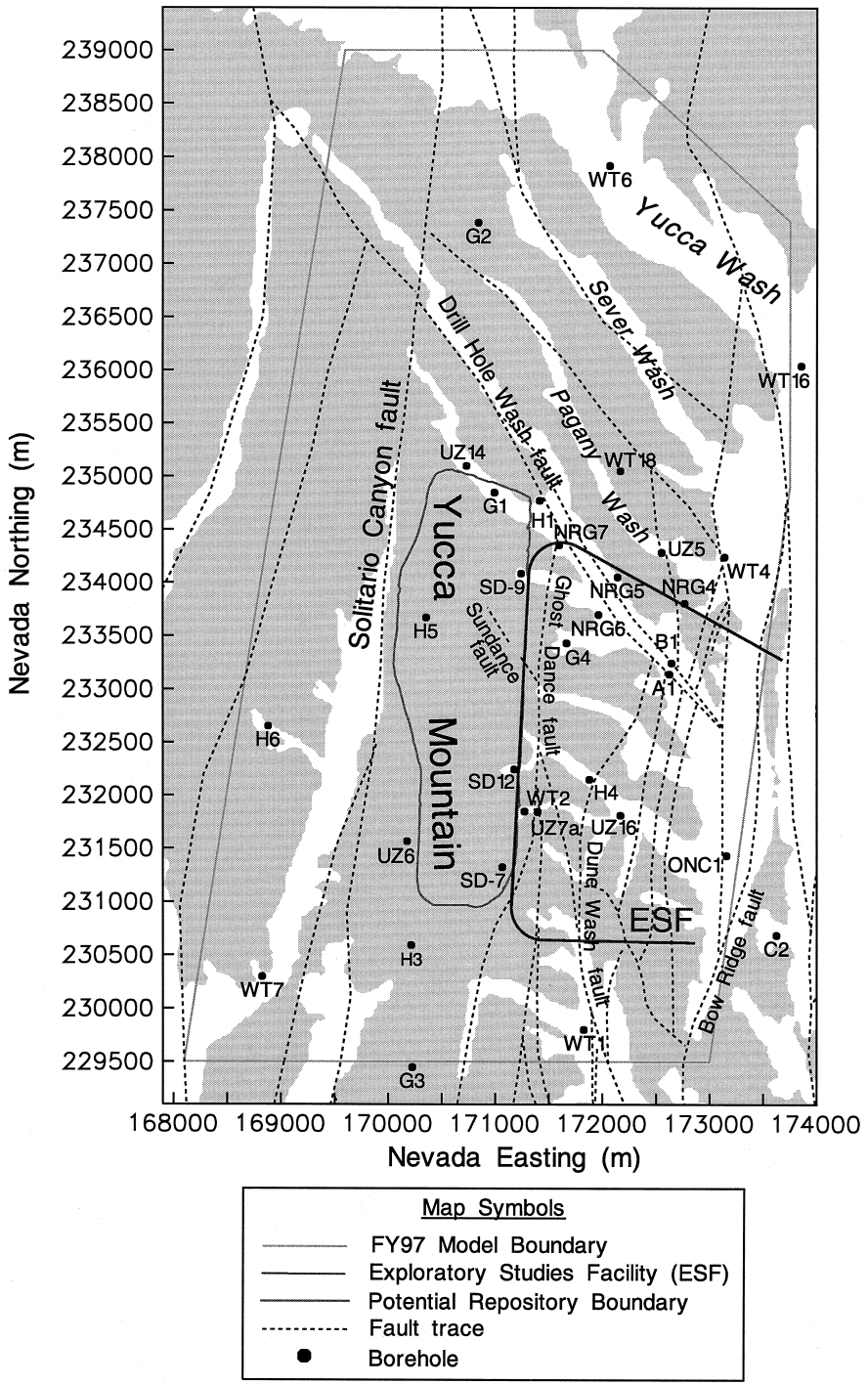
Nevada Northing (m)
239000
238500
238000
237500
237000
236500
236000
235500
235000
234500
234000
233500
233000
232500
232000
231500
231000
230500
230000
229500
168000 169000 170000 171000 172000 173000 174000
Nevada Easting (m)
WT6
Yucca Wash
G2
Drill Hole Wash fault
Sever Wash
Pagany Wash
WT16
Solitario Canyon fault
UZ14
WT18
G1
H1
NRG7
UZ5
WT4
Yucca
SD-9
Ghost Dance fault
NRG5
NRG4
Sundance fault
H5
NRG6
B1
G4
A1
Mountain
H6
SD12
H4
WT2
UZ7a
UZ16
UZ6
ONC1
SD-7
Dune Wash fault
ESF
C2
H3
WT7
Bow Ridge fault
WT1
G3
Map Symbols
FY97 Model Boundary
Exploratory Studies Facility (ESF)
Potential Repository Boundary
Fault trace
Borehole

percolation flux at the repository will also depend on any lateral flow diversion. For example, lateral flow due to capillary barrier effects has been proposed within or at the contacts of bedded tuffs in the Paintbrush Hydrogeologic Unit that overly the potential repository (Montazer and Wilson, 1984). The finding of perched water bodies has given indications that lateral flow along dipping beds may increase the water travel time to the SZ, as well as provide a possible site for dilution (Rousseau et al., 1996).

The infiltration flux has also been estimated using geochemical and isotopic systems (Fabryka-Martin et al., 1994; Johnson and DePaolo, 1994; Meijer, 1995; Flint et al., 1996; Triay et al., 1996; Yang et al., 1996a,b; Fabryka-Martin et al., 1997; Paces et al., 1997; Sonnenthal et al., 1997a,b; Weeks, 1997). While providing constraints on the infiltration fluxes, the latter studies have not considered the transient effects of mixing, and climate changes for a 3-D flow system. Recent 3-D hydrological models have employed chloride, sulfate, and 'background' [1] $^{36}Cl/Cl$ ratios (Robinson et al., 1996, 1997) and have provided important bounds on the transport time and flow pathways, but have not examined in detail the effects on concentrations due to the significant climate changes that have taken place since the last glacial maximum about 20,000 years ago. Subsurface thermal profiles have also been used to bracket the possible range in infiltration rates (Bodvarsson et al., 1997; Sonnenthal and Bodvarsson, 1998), but because thermal diffusivity is much greater than molecular diffusivity, the sensitivity of temperature profiles to infiltration rates is less than that of chloride and strontium variations.

The distribution of chloride in UZ waters is important because it can also allow us to perform sensitivity studies regarding the interaction of fluids flowing in fractures with porewaters in the matrix (i.e., 'fracture–matrix interaction'). Under transient flow conditions, limited equilibration of water in fractures with less mobile matrix porewaters is likely to result in different chloride distributions from those assuming hydraulic equilibrium between fractures and matrix. However, estimates of the effective 'connection areas' for fracture–matrix interaction have differed by several orders of magnitude (see Bandurraga and Bodvarsson, 1997 for a more complete discussion). Another unknown is the extent of evapotranspiration and interaction with soils experienced by waters traveling more rapidly through the fracture system compared to waters infiltrating through the matrix. Therefore, dual permeability models that include variations in the fracture–matrix connection area allow for a more realistic incorporation of flow phenomena in the UZ, but are poorly constrained at present. Therefore, in this work, we use 3-D ECM simulations to characterize the large scale behavior of chloride and strontium in the UZ, with two-dimensional (2-D) dual permeability simulations to assess some of the possible effects of disequilibrium between fractures and matrix on chloride distributions.

The $^{36}Cl/Cl$ ratio has been used to infer the ages of waters at depth ('background' $^{36}Cl/Cl$), and to locate regions of exceptionally rapid flow ('fast-paths') where waters

[1] The term 'background' $^{36}Cl/Cl$ ratio generally refers to those values below 1250×10^{-15} (Fabryka-Martin et al., 1996) and which have no component of ^{36}Cl due to recent fallout from atmospheric testing of nuclear weapons.

less than 50 years old have penetrated, carrying elevated levels of ^{36}Cl and ^{3}H derived from atmospheric nuclear weapons testing ('bomb-pulse'; Fabryka-Martin et al., 1994, 1996, 1997). Because of the strong variability (in time and space) in total chloride in porewaters and in surface infiltrating waters, and subsequent effects of mixing, $^{36}Cl/Cl$ ratios in porewaters are strongly dependent on the spatial distribution of chloride. In this study, we will present results on chloride distributions that should be considered in models of the evolution of $^{36}Cl/Cl$ ratios in the UZ.

Strontium concentrations are related to the infiltration rate (by evaporation), the dissolution of minerals in surface deposits, reaction with minerals or glass in the tuffs, precipitation and dissolution of calcite, and ion exchange with other cations in clays and zeolites. The effect of tuff dissolution on Sr concentrations would be minor compared to the effects of evaporation, based on reaction rates inferred from models of the Sr isotope geochemistry (Marshall et al., 1997; Sonnenthal et al., 1997b). The effect of calcite dissolution or precipitation is unknown, although given an average Sr concentration of about 100 ppm in calcite at the level of the planned repository (Vaniman and Chipera, 1996), there is certainly some Sr loss to calcite in the UZ. Transport models for Sr may indicate how important this effect is and whether the Sr loss due to calcite precipitation may be roughly balanced by Sr gained from tuff dissolution.

Strontium isotopic ratios in porewaters can be affected directly through mineral dissolution and ion exchange, and indirectly through the change in total dissolved Sr concentration resulting from mineral precipitation along flow paths (i.e., a strong reduction in Sr concentration in the water by mineral precipitation can result in waters that are more likely to be isotopically modified in later water–rock interaction). Although some work has suggested that strong shifts in the $^{87}Sr/^{86}Sr$ ratio of porewater in the Paintbrush nonwelded tuffs may be due to dissolution of volcanic glass (Marshall et al., 1997; Sonnenthal et al., 1997b), and lesser shifts due to interaction with the devitrified tuff (Paces et al., 1997), the total porewater strontium concentration may not have been affected enough to change the concentrations markedly. For the purpose of this study, the latter statement is taken as a testable hypothesis and not necessarily an assumption of the model. Except for the perched water bodies, there are very few measurements of Sr in porewaters from the UZ to test this hypothesis. Detailed comparisons to the modeling results should therefore be performed when further data become available. Because of the limited data on $^{87}Sr/^{86}Sr$ isotopic ratios and Sr concentrations in porewaters, we do not present model results for this system; however, as new data become available, there is a potential for gaining very useful constraints on infiltration and flow patterns in the UZ.

2. Geologic features

The geology of Yucca Mountain is described in detail elsewhere (Buesch et al., 1995). For the purpose of this paper, we define here the major hydrogeologic units that form the basis for discussion of chemical variations. An E–W cross-section through the Yucca Mountain showing the major hydrogeological units in the LBNL SSM is depicted in Fig. 2 (Haukwa and Wu, 1997). The welded tuff outcropping in many areas at the

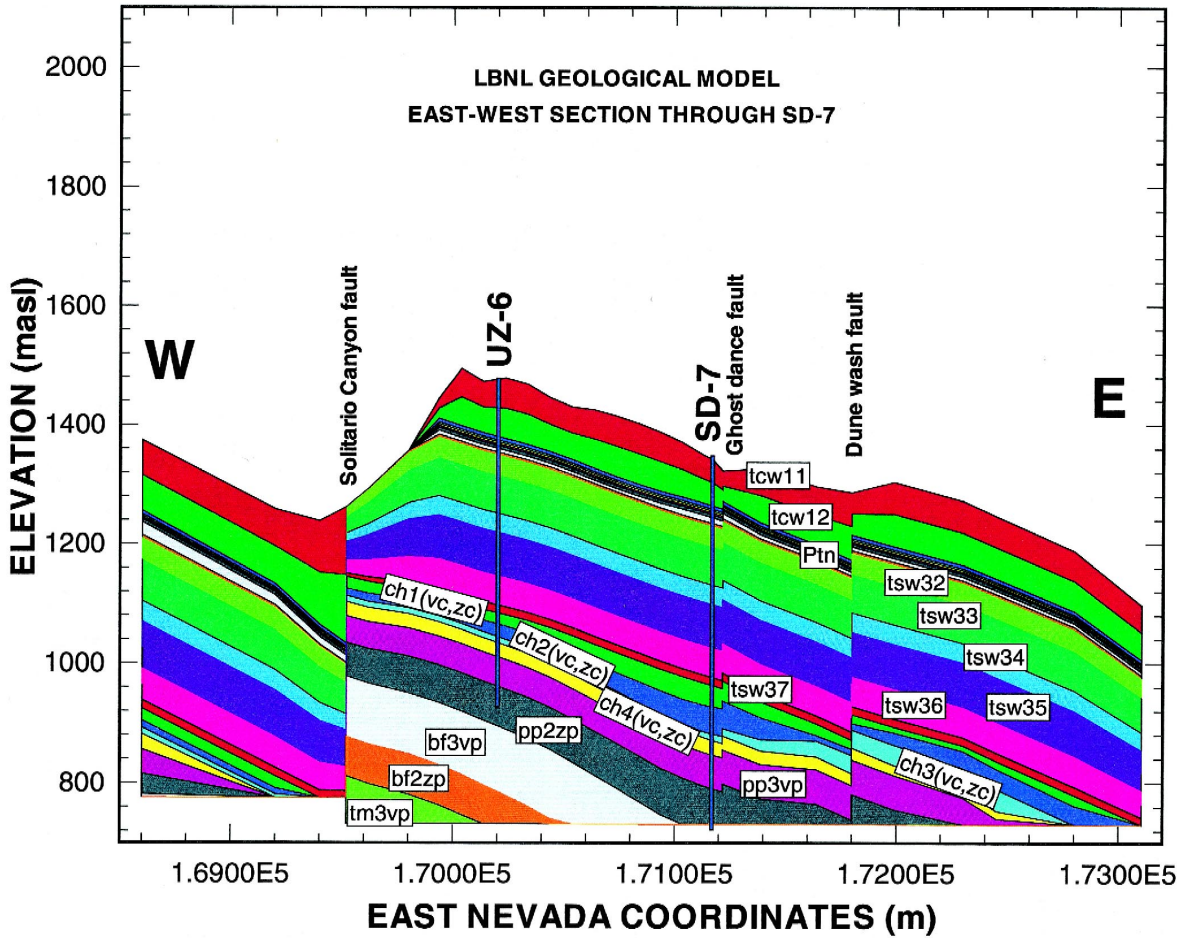

Fig. 2. East–West cross-section through Yucca Mountain showing LBNL UZ SSM layers, major faults, and borehole locations (Haukwa and Wu, 1997).

surface is termed the Tiva Canyon tuff (TCw). Because of their similar hydrological properties, the nonwelded base of the Tiva Canyon tuff, all of the poorly welded and bedded units directly below it (Yucca Mountain tuff and Pah Canyon tuff), and the top nonwelded portion of the Topopah Spring tuff are treated as a single major hydrogeologic unit, the PTn. The welded interior of the Topopah Spring tuff is termed the TSw. Nonwelded Topopah Spring tuffs at the base of the welded unit are combined with the uppermost nonzeolitized bedded tuffs of the Calico Hills tuffs to form the uppermost hydrogeologic unit of the CHn. Some zeolitized tuffs are also distinctly recognized as part of the CHn. Below the CHn, several units just above and intersecting the water table comprise the Prow Pass (PPn) and Bullfrog tuffs (BF).

3. Chloride and strontium chemistry of waters

3.1. Chloride concentrations in precipitation and surface chloride fluxes

Modeling the chloride distribution requires that its concentration in infiltrating water or its total surface flux be known. The chloride flux includes dissolved material in rain, particulates in snow, and a contribution from windblown dust (Meijer, 1995; Fabryka-Martin et al., 1996, 1997; Triay et al., 1996; Tyler et al., 1996). Estimates of the chloride content in precipitation at Yucca Mountain have been inferred from measurements at other nearby locations, such as the Kawich Range (McKinley and Oliver, 1994, 1995; Triay et al., 1996; Table 1). Triay et al. (1996) obtained a mean chloride concentration in precipitation of 0.55 mg/l, which is probably close to the minimum value expected. A present day surface flux of 106 mg/m^2 year was used by Fabryka-Martin et al. (1996) for the Yucca Mountain area. Combining the mean annual precipitation of about 170 mm/year calculated for Yucca Mountain (Flint et al., 1996) with the chloride flux given by Fabryka-Martin et al. (1996) yields a mean chloride concentration of about 0.62 mg/l (Fabryka-Martin et al., 1997). We refer to this concentration as the 'effective concentration', because it includes a windblown dust component.

The contribution from windblown dust may be 33% of the total chloride flux in the Great Basin of Nevada and Utah (Dettenger, 1989; Tyler et al., 1996). Even though the contribution from windblown dust is considered in the flux given by Fabryka-Martin et

Table 1
Chloride concentration in precipitation and estimates of the surface chloride flux at Yucca Mountain and nearby areas

Type	Location	Chloride	Reference
Precipitation	Kawich Range	0.55 mg/l	McKinley and Oliver (1994), McKinley and Oliver (1995), Triay et al. (1996)
Surface flux	Yucca Mountain	106 mg/m^2 year	Fabryka-Martin et al. (1996)
Effective concentration	Yucca Mountain	0.62 mg/l	Fabryka-Martin et al. (1997)

al. (1996), and in part in the measured precipitation, we can bound the upper limit of concentration by adding 33% more chloride to the 0.55 mg/l concentration to yield a maximum of about 0.73 mg/l. This upper bound is useful, because as the effective chloride concentration increases, the infiltration rate necessary to maintain the same chloride concentration after evapotranspiration must also increase. Thus, by bounding the concentration at the higher end, we set an upper limit on the infiltration rate. Also, the upper limit is less well defined than the lower limit, which is more easily set from the concentrations in precipitation. Clearly, this variation in effective chloride concentration (before evapotranspiration) is much less than the over an order-of-magnitude range in estimates of infiltration rate, and therefore the surface chloride concentration is a moderately well-constrained boundary value for modeling studies. The rough upper bounding effective concentration is used only for consideration of its possible effect on the interpretation of the infiltration rates calculated from measured chloride concentrations, precipitation and infiltration rates. In the modeling studies, only the reported 0.55 and 0.62 mg/l effective concentrations were used.

Temporal variations in the effective chloride concentration are also be important for modeling the long-term chloride evolution. Although there is some evidence for elevated chloride concentrations in ice cores from Greenland, such shifts may have been due to changing climatic patterns, which do not seem to have affected the Great Basin during this period (Tyler et al., 1996). Fabryka-Martin et al. (1996) indicated that the surface flux during the Pleistocene was perhaps 30% lower than today, due to the absence of windblown dust from dry lake beds. For this study, we assume that the effective chloride concentration during the last glacial maximum was the same as today.

3.2. Strontium concentrations in precipitation

The concentration of strontium in precipitation has been given as 5.8 μg/l by Triay et al. (1996). The effective concentration, including windblown dust, is unknown, and because of the extremely low concentration of Sr in precipitation it could be affected very strongly by soluble aerosols. There are apparently no systematic studies of the $^{87}Sr/^{86}Sr$ ratio in precipitation to determine the influence of aerosols, although aerosols derived from Paleozoic carbonates with $^{87}Sr/^{86}Sr$ ratios close to modern seawater (~ 0.709; Faure, 1977) may not change the isotopic ratio of the precipitation significantly from its original composition as derived from sea spray. For the present modeling, we use the strontium concentration in precipitation as input data and compare the modeled concentrations to subsurface measurements.

3.3. Chloride concentrations in the UZ

Chloride concentrations in porewaters from boreholes have been reported by Yang et al. (1988, 1996a,b), and more recently in porewater samples collected from the ESF tunnel (Fabryka-Martin et al., 1998). Because of difficulties in extracting porewaters from low porosity welded tuffs, chloride concentrations from the UZ are limited mostly to the nonwelded portion of the Tiva Canyon tuff, the underlying Paintbrush bedded tuffs, the top nonwelded zone of the Topopah Spring Hydrogeologic unit, the Calico Hills unit, and underlying geologic units.

3.3.1. Chloride concentrations in the Tiva Canyon welded and Paintbrush bedded tuffs

The water compositions (calcium chloride/sulfate) in the TCw and PTn are characteristic of interaction with near-surface soils (Yang et al., 1996a). Porewater chloride concentrations in the PTn are highly variable (45 to 245 mg/l in Borehole UZ-14 and 47 to 185 mg/l in Borehole NRG-6) with the highest concentrations in those samples located at the top of this unit (Fig. 3). In Borehole SD-9, where only two measurements were reported, the upper sample has a chloride concentration of 170 mg/l, underlain by a value of 93 mg/l. Chloride concentrations of 77.2 and 49.6 mg/l were measured in PTn porewaters from Boreholes SD-7 and SD-12, respectively. Recent measurements from the ESF (Fabryka-Martin et al., 1998) have yielded concentrations ranging from 10 to 69 mg/l; their generally lower concentrations compared to those from earlier studies is suggested by the latter authors to be the result of sampling under regions of higher infiltration. In the North Ramp of the ESF, chloride concentrations also show the trend of higher concentrations near the top of the PTn, with much lower concentrations at greater stratigraphic depth. Any trend in the South Ramp cannot be confirmed, owing to fewer samples, a thinner geologic section, and faulting; however the sample from the uppermost PTn layer in this section has the highest chloride concentration.

The strong vertical heterogeneity in the PTn porewater chemistry has been ascribed to lateral transport (Yang et al., 1996a), although roughly similar concentration profiles have been observed in vadose zones elsewhere at the Nevada Test Site (NTS) (Tyler et al., 1996). In the Area 5 Waste Management Site at the NTS investigated by Tyler and others there is a high near-surface concentration that drops off sharply. This trend is

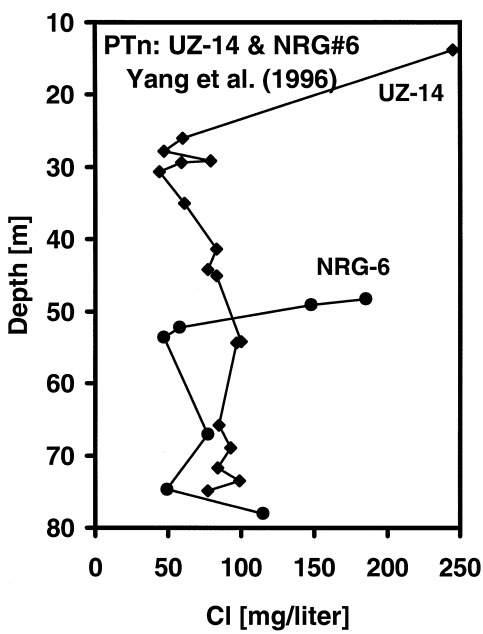

Fig. 3. Chloride profiles in the PTn from Boreholes UZ-14 and NRG-6. Data from Yang et al. (1996a).

characteristic of many desert soil profiles in the Great Basin and Desert Southwest, and has been attributed to a cessation of recharge to the water table between 13 and 15 ka (Tyler et al., 1996). Although the modern arid climate has lasted approximately 10 ka, precipitation may have been higher until about 5 ka (Tyler et al., 1996).

In two of the boreholes investigated by Tyler et al. (1996), another broad peak in chloride concentration is found several tens of meters below the upper one (Fig. 4). The deeper second chloride hump was suggested to have formed prior to 50 ka, followed by a period of recharge. However, ^{14}C ages from porewaters ranged from 11 to 15 ka, much less than the chloride 'ages', based on transport calculations assuming one-dimensional (1-D) plug flow. One borehole did not show this second hump (plot not reproduced here; see Tyler et al., 1996), possibly because of recharge about 25 to 35 ka. Samples taken from this borehole had a range of ^{14}C ages of 14 to 17 ka. These seemingly young ages were attributed to gaseous CO_2 diffusion. Differences in ^{14}C ages of porewater and those inferred from $^{36}Cl/Cl$ ratios are also seen in the PTn, where ^{14}C ages of 1000 to 4900 years were obtained from boreholes at Yucca Mountain (Yang et al., 1996a), and elevated background $^{36}Cl/Cl$ ratios indicating a component of Pleistocene-age water are present in the ESF (Levy et al., 1997).

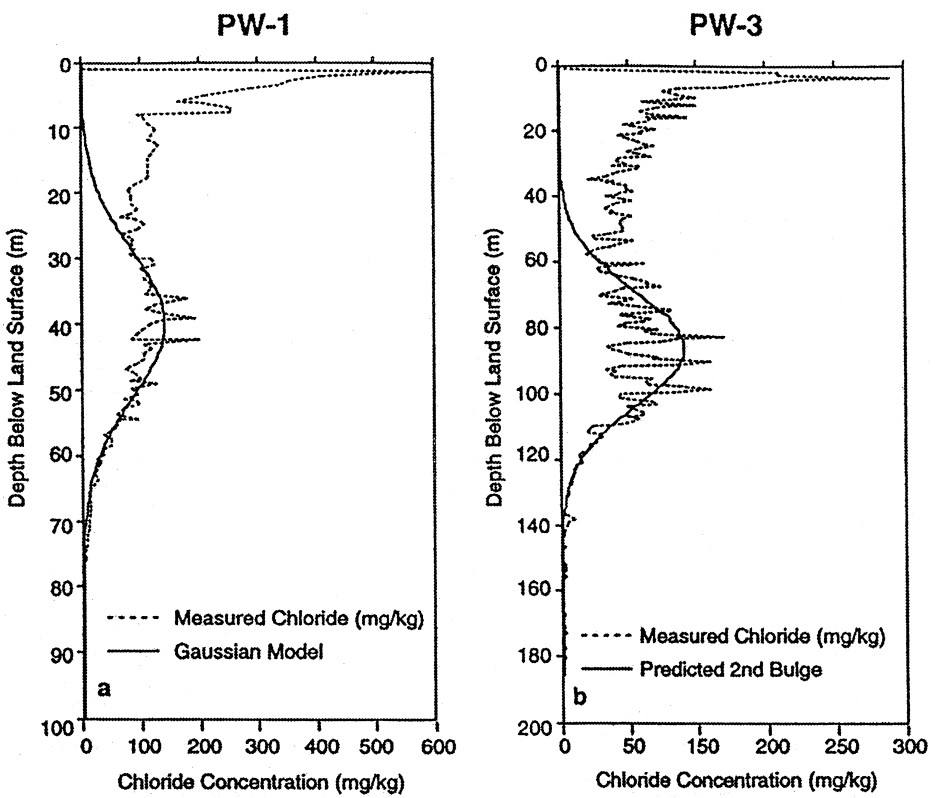

Fig. 4. Chloride concentrations in alluvial soils (mg/kg) in boreholes from thick soil zones at the NTS (Tyler et al., 1996).

Tyler et al. (1996) considered the system as 1-D, with the profiles generally reflecting a history of climate changes and recharge. Because of the exceptionally thick soil zone ($\sim 200+$ m) and the extremely low infiltration rate at the site of the investigation, evidenced from the lack of bomb-pulse $^{36}Cl/Cl$ ratios below about 2 m depth (Tyler et al., 1996), a direct comparison to the PTn under Yucca Mountain is not justifiable. However, because the PTn has few fractures (Sweetkind et al., 1997) and flow is thought to be confined predominantly to the matrix (Montazer and Wilson, 1984), the mode of transport of Cl through it should be roughly similar to thick alluvium, and therefore similar profiles of those observed by Tyler et al. (1996) could be present. In Borehole UZ-14, the distance between the top chloride peak and the center of the second chloride increase is about 40 m (Fig. 3), similar to the spacing observed in the PW-1 borehole shown in Fig. 4. If one takes the high concentration seen at the base of NRG-6 (Fig. 3) as the position of the second chloride bulge, then the peak-to-peak distance in this profile is about 30 m. Thus, there is some similarity between the NTS profiles and the PTn chloride profiles.

An explanation for the high concentrations at the top of the PTn involving evaporation of water by air circulating in the overlying highly permeable fractured TCw unit has been offered by Patterson et al. (1996). However, such evaporation should have affected all of the concentrations in the subsurface as these waters also migrated through the PTn, simply resulting in a shift in the Cl profile. Based on studies of the cation ratios, Yang et al. (1996b) concluded that there is little evaporation in the PTn and in underlying units, and that some elevated cation concentrations were the result of water–rock interaction.

Given the possibility of lateral flow in the PTn (Montazer and Wilson, 1984; Rousseau et al., 1996), and the potential interaction of higher velocity water traveling through fractures with slow-moving matrix porewater, any climatic signal in the water chemistry may have also been wiped out. Although the apparent ages of water in the PTn by ^{14}C (Yang et al., 1996a) and models using the current infiltration rate (Bandurraga et al., 1997) are consistent with a few thousand years travel time through the PTn, the similarity in the chloride profiles to those elsewhere in the NTS deserves further attention.

In addition to the effects of climate and local mixing processes, spatial heterogeneities in the porewater compositions are affected by differing degrees of evapotranspiration. It would be expected that chloride (and other conservative solutes) should have lower concentrations in regions below thin soil and higher concentrations beneath thick alluvial deposits, assuming that little surface runoff has taken place. Although there are insufficient analyses from boreholes in regions of high and low infiltration to test this hypothesis, chloride concentrations were measured in porewaters taken from cores in Boreholes UZ-4 and UZ-5 which are located within a low infiltration region in Pagany Wash and in an area of a higher infiltration rate at the edge of Pagany Wash, respectively. Except for one sample taken at a greater depth in UZ-5, the chloride concentrations in the PTn porewaters in UZ-4 are roughly twice those of UZ-5; however, there are insufficient data as a function of depth to use this as other than possible corroborating evidence. More detailed discussion and plots of chloride concentrations in the individual boreholes are presented in conjunction with the modeling studies presented later in this paper.

The overall conclusion from this qualitative examination is that some effects of the climate change that occurred about 10 ka are probably preserved in places in the PTn (as suggested by the greater-than-modern $^{36}Cl/Cl$ ratios in the North Ramp of the ESF and the chloride variations observed in boreholes) but that porewaters in most areas have been replaced by Holocene recharge.

3.3.2. Chloride concentrations in the Topopah Spring tuff

Analyses of chloride concentrations in porewaters from the Topopah Spring unit are mostly restricted to the nonwelded top, with some recent measurements in samples from the upper lithophysal horizon of the TSw in the South Ramp of the ESF, and these range from 17 to 150 mg/l (Fabryka-Martin et al., 1998). It could be inferred from the extremely low matrix permeability of the TSw that areas of low infiltration and/or low fracture connectivity should retain some porewaters greater than 10,000 years old. Regions of high infiltration, however, may have been flushed completely over the past 10,000 years.

3.4. Perched water and SZ chloride concentrations

Chloride concentrations in water samples collected during pump tests in the perched water bodies (Table 2) are less variable and much lower than in matrix porewater from the UZ, tentatively suggesting that the water is fairly well mixed or that it is derived from a relatively homogeneous source. The exceptions are porewaters from UZ-14, which have slightly higher and more variable chloride concentrations that are similar in overall aqueous chemistry to porewater from the Topopah Spring tuff (Yang et al., 1996a).

Several hypotheses have been set forth for the origin of the perched water bodies at Yucca Mountain. δD and $\delta^{18}O$ values indicate that the perched water has undergone very little evaporation before infiltration, is only slightly heavier than SZ water (Yang et al., 1996b), but is unlike isotopically lighter Pleistocene-age water. Based on the inferred postglacial $\delta^{18}O$ and δD isotopic values, corrected ^{14}C water residence times, and lack of equilibration with ^{14}C in the gas-phase in overlying units, Yang et al. (1996b) suggest

Table 2
Mean chloride concentrations in perched water and in the SZ (Yang et al., 1996a,b except as noted)

Borehole	Cl range (mg/l)	Average Cl (mg/l)
NRG-7A	–	7
UZ-14	6.7–15.5	8.6
SD-7	4.1–4.4	4.2
SD-9	–	5.6
ONC#1[a]	–	7.1
USWG-2[b]	–	6.5
J-13[a]	–	7.14[c]

[a] Saturated zone.
[b] Uncertain if SZ or perched water.
[c] Harrar et al. (1990).

that the perched water is likely to have formed through rapid fracture flow, with little interaction with matrix porewaters, and with residence times of between 2000 and 6000 years.

An alternative explanation is that the perched water represents, in part, a remnant of Pleistocene-age water emplaced when precipitation rates were higher, with their compositions reflecting some mixing of Holocene infiltration. Effective chloride concentrations may have been lower because dry lake beds were water-filled during these periods, thus lessening windblown chloride at Yucca Mountain (Fabryka-Martin et al., 1996). The cooler and wetter climate would also have resulted in much higher infiltration fluxes (Flint et al., 1996). Some support for a significant proportion of Pleistocene water in the perched water bodies comes from a comparison of $^{36}Cl/Cl$ ratios and ^{14}C activities which indicate apparent ages of up to 8 to 12 thousand years (Robinson et al., 1997). Although nearly all aqueous and gaseous ^{14}C apparent ages from the TSw and Calico Hills units are less than 10,000 years old, air and water contamination during drilling may have resulted in anomalously young ages (Yang et al., 1996b). On the other hand, dissolution of carbonates would shift the apparent ages to older values (Yang et al., 1996b).

3.5. Strontium concentrations and isotopic ratios

Only a handful of analyses were available (at the time of this study) of the Sr content of porewaters at Yucca Mountain (Table 3). One sample in the PTn from Borehole UZ-5 and six samples from the PTn in UZ-4 were analyzed by Yang et al. (1988). Some samples of perched water were analyzed for Sr and $^{87}Sr/^{86}Sr$ in Boreholes NRG-7A, SD-9, and UZ-14 (Rousseau et al., 1996).

These few UZ porewater Sr concentrations are considerably higher than those in the perched water; however, the perched water bodies can be broken into two distinct compositional types. Sr concentrations in WT-24 and UZ-14 are relatively high, while those in SD-7, SD-9, and NRG-7A are very low, even though chloride concentrations in these waters are similar. The only plausible explanation is that ion exchange with calcium-rich zeolites may have depleted some of the perched water bodies in Sr. This is supported by the fact that the perched water bodies in UZ-14 and WT-24 are perched on

Table 3
Mean strontium concentrations and isotopic ratios in porewater and perched water (Yang et al., 1988; Rousseau et al., 1996; Marshall personal communication; Patterson et al., 1998)

Borehole	Sample type	Sr (μg/l)	$^{87}Sr/^{86}Sr$
UZ-4	porewater	1211	n.a.[a]
UZ-5	porewater	563	n.a.
NRG-7A	perched water	5	0.71269
SD-9	perched water	3	0.71340
SD-7	perched water	11	0.71175
UZ-14	perched water	240	0.71236
WT-24	perched water	169	0.71206

[a] Not analyzed.

the basal vitrophyre of the TSw (Rousseau et al., 1996; Patterson et al., 1998), and not on the strongly zeolitized Calico Hills units. The Sr isotopic ratios in the perched water bodies vary significantly but are still similar to the range of calcite and porewater $^{87}Sr/^{86}Sr$ ratios and significantly lower than most of the bulk rock ratios in the TCw, PTn, and TSw units (Paces et al., 1996, 1997).

4. Conceptual model of chloride and strontium geochemistry

Clearly, large differences exist between the chloride concentrations in waters sampled from the PTn, TSw and the perched water bodies. The likely explanation for such variations is that they represent waters that have undergone differing degrees of evaporation, interaction of waters flowing through fractures and the matrix porewaters, and large-scale mixing via lateral flow (Fig. 5). The chloride concentration distribution is that of lower chloride concentrations at higher elevations in regions of high infiltration, and high chloride concentrations underlying thick alluvium where evapotranspiration is highest. Low-lying areas may also have less precipitation than ridgetops, and therefore receive a smaller chloride flux, but still have higher concentrations in porewaters because of the greater amount of evaporation. Substantial evaporation of precipitation is also implied by the abundant calcrete at Yucca Mountain (Vaniman and Whelan, 1994). In addition to surface evaporation, air flow through the highly fractured Tiva Canyon welded tuff may have caused further evaporation (Patterson et al., 1996) that is spatially variable and higher where dry downdrafts prevail. The effect of a locally higher infiltration rate owing to increased infiltration during a past wetter climate and the effect of mixing of lower concentration waters from areas of higher infiltration via

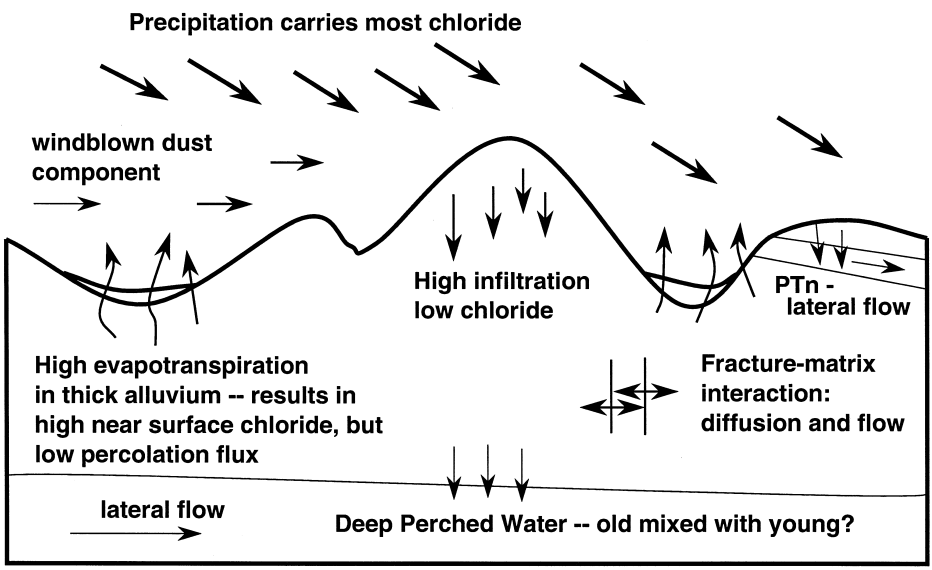

Fig. 5. Schematic diagram showing major processes affecting the chloride chemistry at Yucca Mountain.

lateral flow (e.g., water entering ridgetops and side slopes mixing with infiltration under alluvium-filled channels) is, however, indistinguishable from analysis of the chloride concentrations alone. The amount of mixing at depth will also depend on the degree to which equilibration takes place between waters traveling rapidly through fractures and less mobile matrix porewaters.

To model the large variation in the porewater chloride and strontium concentrations in the UZ, we must account for waters that have undergone differing degrees of evapotranspiration, in addition to spatial and temporal variations in the surface fluxes of these components. Whereas precipitation may vary spatially from 130 to 250 mm/year around Yucca Mountain (Flint et al., 1996), resulting in roughly equivalent variations in the chloride flux, infiltration is thought to vary by a few orders of magnitude, from zero in areas of thick alluvium to several tens of millimeters per year on high elevation side slopes. Owing to the fairly simple behavior of the chloride ion in the subsurface, compared to other aqueous species that may be strongly affected by water–rock interaction, we can use these spatial differences in evapotranspiration to estimate the chloride concentrations of waters entering the UZ. Section 4.1 establishes the basic equations describing the chloride fluxes and concentrations.

4.1. Governing equations

In the following, we consider chloride to be a trace element that is not affected by partitioning into a mineral or vapor phase. During evaporation, the concentration of a trace element i in the liquid (C_i) changes according to the Rayleigh distillation law:

$$\frac{C_i}{C_{i,\mathrm{o}}} = F^{D-1}, \tag{1}$$

where $C_{i,\mathrm{o}}$ is the initial concentration of i in the liquid [2], and F is the mass fraction of liquid remaining. The distribution coefficient between vapor and liquid, and/or between a solid phase and the liquid, is given as D. For chloride, $D \approx 0$ and therefore:

$$\frac{C_{\mathrm{Cl}}}{C_{\mathrm{Cl,o}}} = \frac{1}{F} \tag{2}$$

The fraction of liquid remaining, F, could also be given by the ratio of the net infiltration flux (J_{I}) to the precipitation flux (J_{P}), assuming that net infiltration (as calculated by Flint et al., 1996) is the difference between precipitation and evapotranspiration:

$$F = \frac{J_{\mathrm{I}}}{J_{\mathrm{P}}}, \tag{3}$$

where the fluxes are in units of mass/time. We assume that the small quantity of

[2] In the discussion of Eqs. (1)–(5), C is given by a mass fraction—mass of Cl per unit mass of water. Elsewhere in this paper, concentrations are given in mg/l.

chloride taken up by plant roots during evapotranspiration is negligible, and under steady-state conditions and instantaneous dissolution would be returned to the porewater

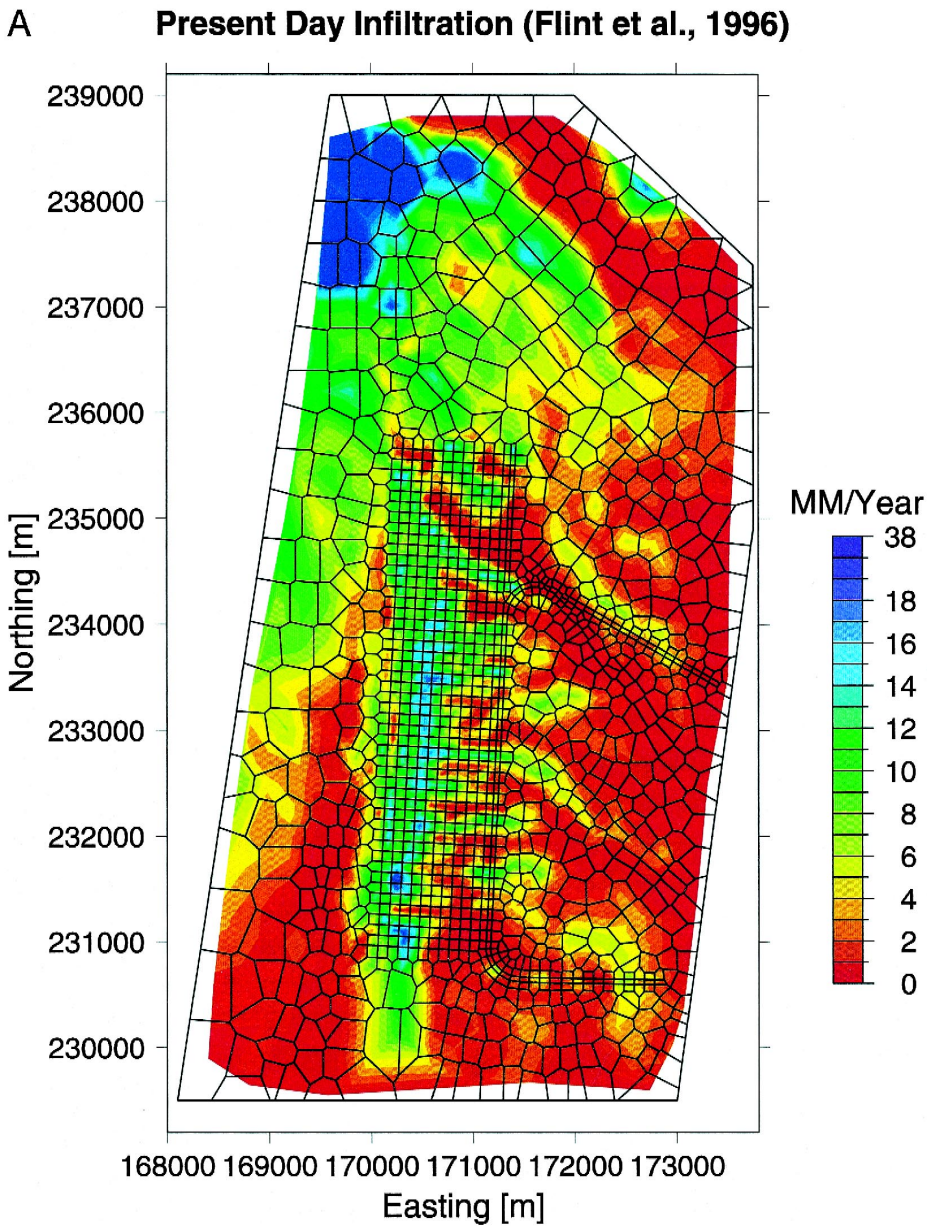

Fig. 6. (a) Modern infiltration distribution from Flint et al. (1996) interpolated onto 3-D model grid. (b) Infiltration calculated for the glacial maximum climate (21 ka) (J. Hevesi, personal communication) and interpolated onto 3-D model grid.

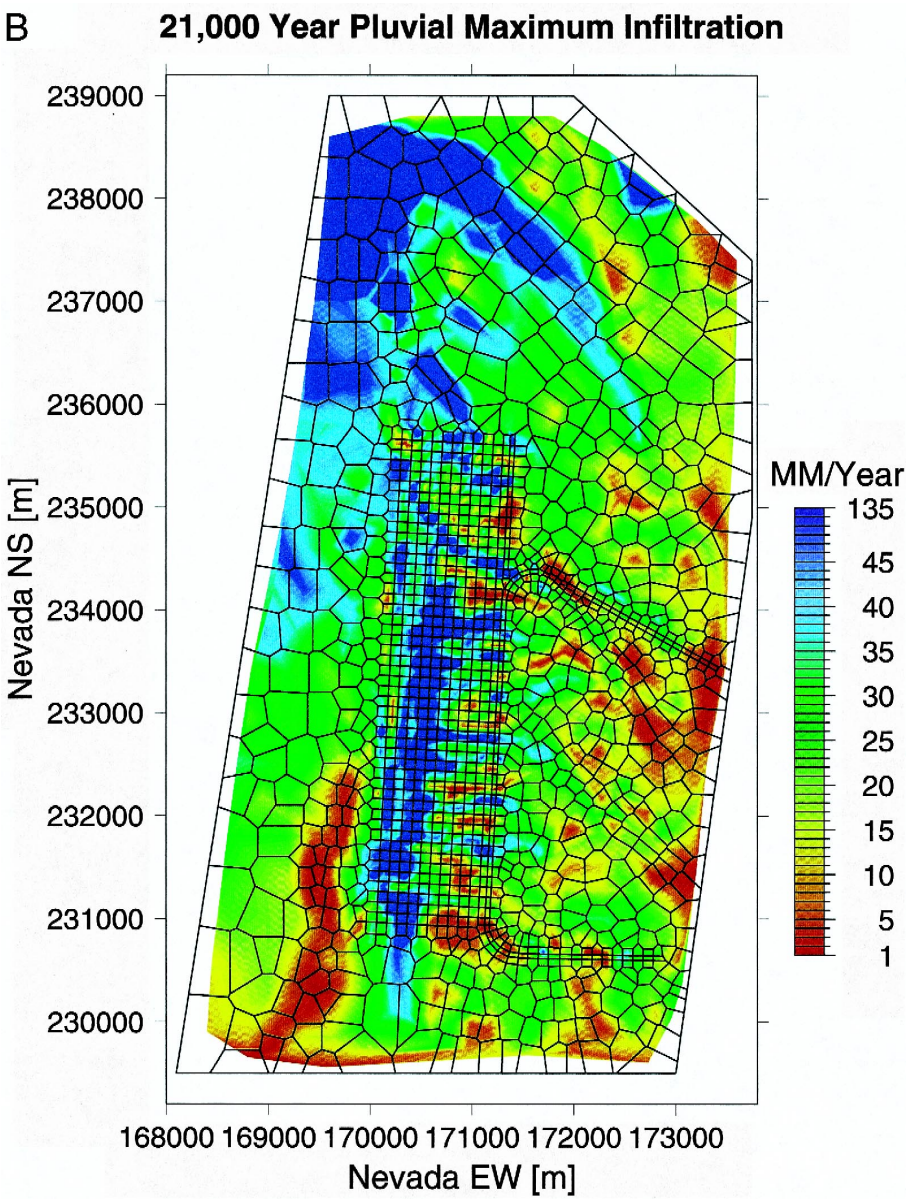

Fig. 6 (continued).

without affecting the chloride mass balance. The concentration of Cl in the infiltration water $C_{\mathrm{Cl,I}}$ is then given by:

$$C_{\mathrm{Cl,I}} = C_{\mathrm{Cl,P}} \frac{J_{\mathrm{P}}}{J_{\mathrm{I}}}, \tag{4}$$

where $C_{Cl,P}$ is the concentration in precipitation. This would lead, however, to infinite concentrations in regions of zero infiltration. Therefore, the boundary condition prescribed is the chloride flux (J_{Cl}):

$$J_{Cl} = C_{Cl,P} J_P . \quad (5)$$

The simulations performed in this report assume that all Cl and Sr are dissolved. Because the maximum Cl concentrations in the model are on the order of a few thousand mg/l in some zero infiltration blocks under thick alluvium-filled washes, they are still below the value at which halite would precipitate from a saline brine ($\sim$ 300,000 mg/l NaCl at 25°C; Holser, 1979).

We consider Sr to behave similarly to Cl in infiltrating waters. In zeolitic rocks, it is assumed that Sr undergoes strong equilibrium exchange, and very little exchange in unzeolitized rocks. We assume that the surface soils and alluvium have reached some steady-state concentration of Sr, so that even though they may act as a reservoir for Sr (plants, carbonates, and sulfates), their degradation and release of Sr into infiltrating water is approximately equal to the surface Sr flux. We also assume that the loss of Sr to fracture calcite in the UZ does not significantly deplete waters in Sr, and that tuff dissolution is too slow to shift concentrations dramatically.

As in the case of Cl, it is expected that large spatial variations due to evapotranspiration at the surface will overwhelmingly control the pattern of concentrations observed in the subsurface. A description of the first-order ion exchange reaction used to model Sr exchange with zeolitic rocks is given by Oldenburg and Pruess (1995) and its implementation in the T2R3D module of TOUGH2 by Wu et al. (1996).

4.2. Spatial variation in near-surface chloride concentrations

The surface chloride fluxes were calculated for Yucca Mountain using the spatially varying precipitation data that have been provided at a 30 m gridblock resolution (Flint et al., 1996). Precipitation and infiltration fluxes were calculated for the 3-D model boundary by averaging all points enclosed in a circular area equivalent to the model grid block surface area. Due to the large differences in gridblock areas, this approach yields fluxes that are more mass-conservative than methods using a single search radius for all gridblocks. Fig. 6a and b shows the contoured infiltration maps superimposed on the 3-D model grid for the modern and 21 ka glacial maximum climates. Fig. 7a and b shows the calculated surface chloride concentrations in infiltration water for the modern and glacial maximum climates interpolated onto the 3-D model grid. The concentration contours generally reflect the inverse of the infiltration—high concentrations in alluvial washes, and lower concentrations along the ridge top of Yucca Mountain and regions to the northwest of the Solitario Canyon Fault, where there is higher precipitation and infiltration.

It is important to consider both the chloride fluxes and concentrations, because areas of higher fluxes (e.g., high precipitation regions) may have lower concentrations owing to increased infiltration, thus less evaporative concentration. Runoff will result in areas with higher surface water fluxes and thus higher chloride fluxes, which could lead to high concentrations in infiltrating water if evapotranspiration is high, or low concentra-

tions if little evaporation takes place and there is a large infiltration event of dilute waters.

Some of the factors that are likely to modify the chloride fluxes and concentrations, which we have not included in the modeling, are:

1. The spatial distribution of the chloride flux from windblown dust, which is likely to be heterogeneous, with low dust accumulation at exposed ridges and greater accumulations in valleys;
2. Surface runoff, which would tend to lessen the chloride flux on side slopes and add it to down slope areas.

The greatest accumulation of salts is likely to be in lower elevation regions, so that the net effect of runoff, wind erosion and deposition will be lower chloride fluxes and concentrations at ridgetops and side slopes, with variable but generally higher fluxes and concentrations in alluvial washes. A large runoff event could flush out porewaters in alluvial washes and leave a long-term signature in the subsurface chloride profile.

5. Modeling methods, parameters, and results

5.1. Numerical codes and methods

Simulations were performed using the TOUGH2 code 'transport of unsaturated groundwater and heat' (Pruess, 1991; Pruess et al., 1996) and the T2R3D version (Wu et al., 1996) of the TOUGH2 code. TOUGH2 is based on the integral finite difference method (Edwards, 1972; Narasimhan and Witherspoon, 1976; Pruess, 1991). The T2R3D version of TOUGH2 takes into account tracer diffusion, dispersion, radioactive decay, and linear first-order adsorption. All simulations utilized the 'equation of state' (EOS3) module of TOUGH2, which solves the conservation equations for air and water simultaneously. All 3-D simulations utilized the 'equivalent continuum method' (ECM; Pruess et al., 1996), which treats the fracture and matrix as a continuum with total capillary pressure equilibrium between fractures and matrix porous medium. The 2-D simulations utilize the dual permeability concept for flow and transport (Pruess, 1991). In all steady-state simulations, the steady-state flow field was simulated first using the EOS3 module of TOUGH2, followed by the coupled water–air-chemical transport simulation using T2R3D, which includes the EOS3 module.

5.2. Hydrologic properties of rock matrix and fractures

Numerous studies have been devoted to the measurement, analysis, and calibration (by inverse methods) of the hydrologic properties of the rock units at Yucca Mountain (Flint and Flint, 1990; Flint et al., 1994; Bandurraga, 1996; Bandurraga and Bodvarsson, 1997; Flint, 1998). Hydrologic properties of individual fractures and the fracture system are treated by Altman et al. (1996), Anna (1997), LeCain (1997), Bandurraga and

Bodvarsson (1997), and Sonnenthal et al. (1997a). A summary of the typical matrix and fracture permeabilities and porosities used in the 3-D ECM simulations is given in

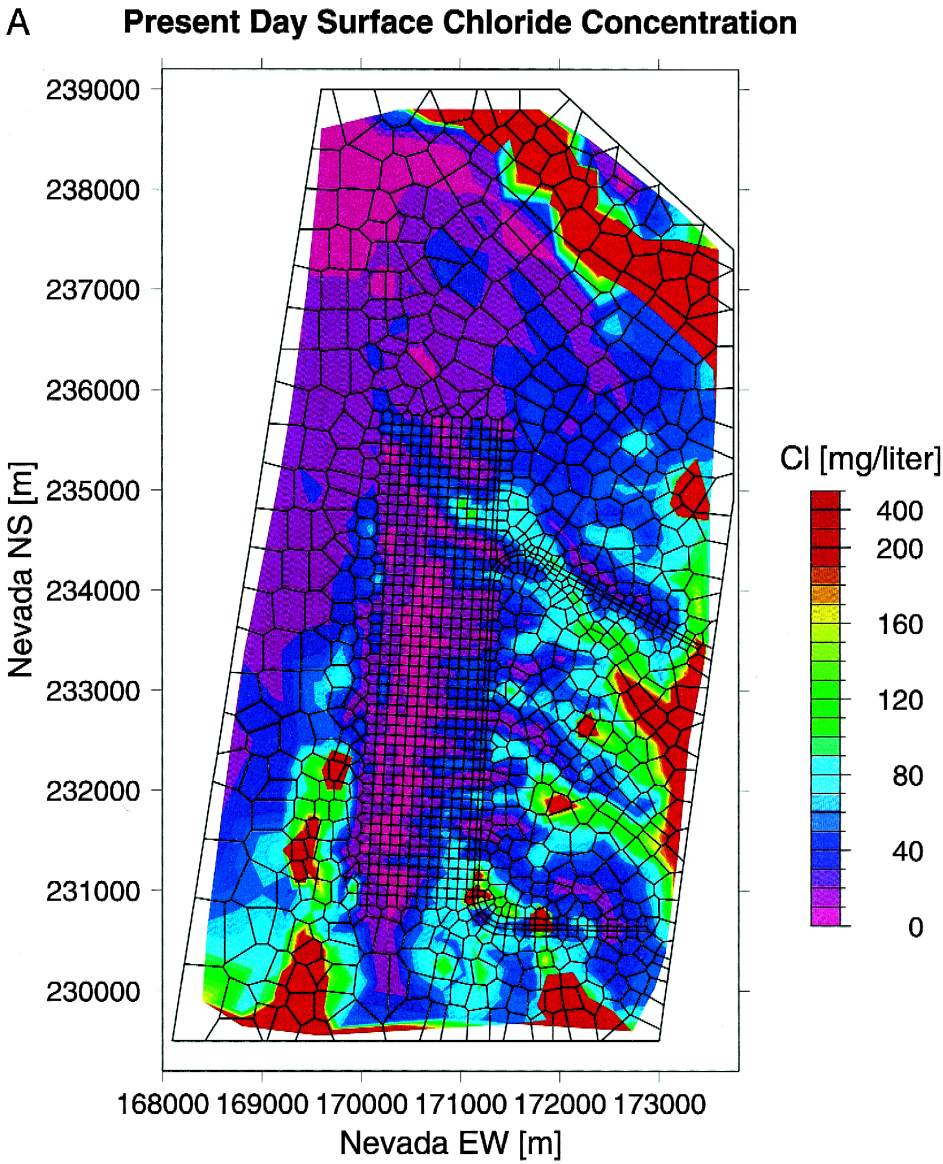

Fig. 7. (a) Steady-state chloride concentrations in uppermost model layer calculated using the effective concentration precipitation of 0.55 mg/l (Triay et al., 1996) and the spatially variable precipitation and infiltration patterns (Flint et al., 1996). The chloride flux from precipitation combined with the infiltration flux of water yields a concentration equivalent to that given by Eq. (4). (b) Chloride concentrations calculated for the conditions of last glacial maximum (21 ka).

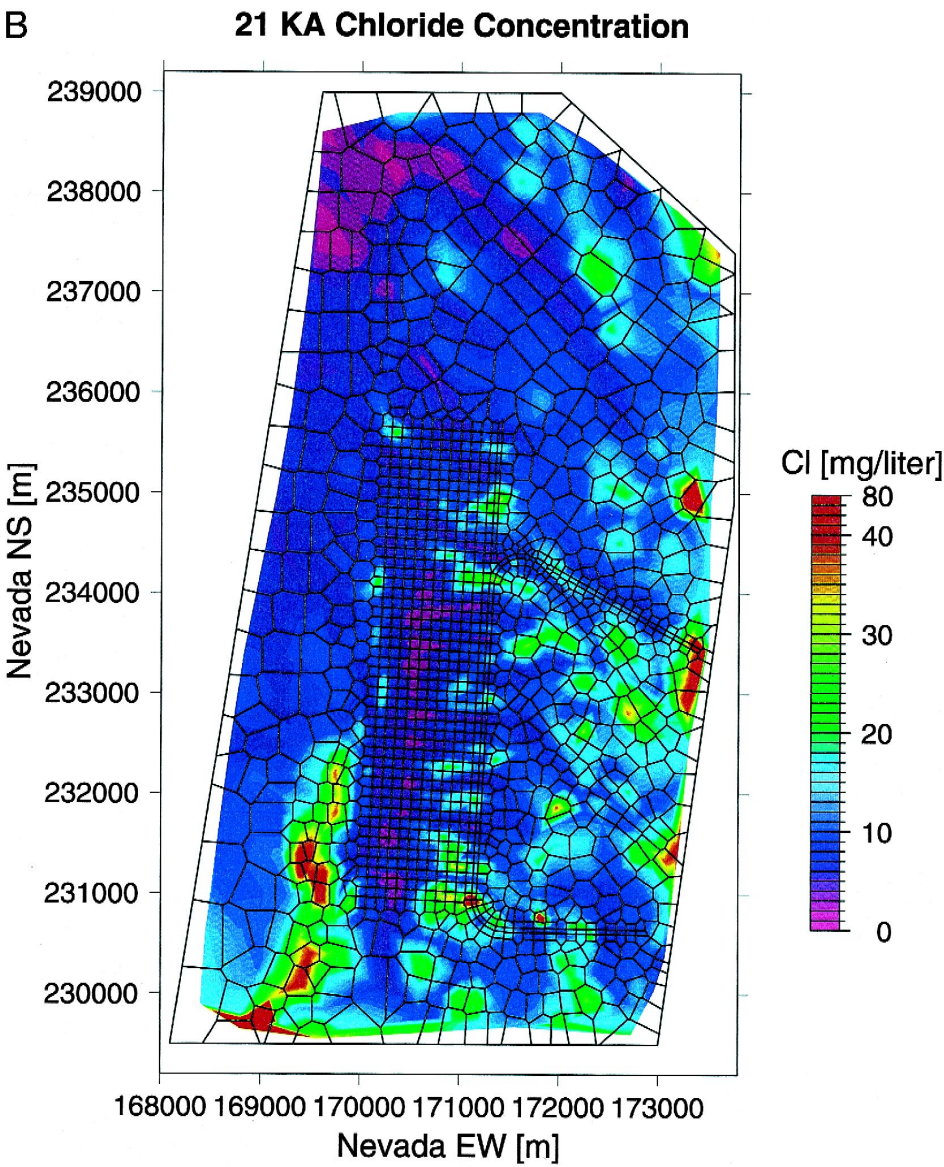

Fig. 7 (continued).

Table 4. The hydrologic properties are set for each modeled rock layer, and for these simulations there are no local spatial variations within a given layer, although some layers are laterally discontinuous. Within the Calico Hills unit, however, some layers are zeolitized over part of the model domain and other areas are characterized by less altered vitric tuffs. Some of the simulations use properties slightly different from those

Table 4
Typical matrix and fracture hydrologic properties for the LBNL 3-D UZ SSM layers at Yucca Mountain

Layer	Geologic unit	κ_f (m^2)	κ_m (m^2)	ϕ_f	ϕ_m	X_{f-m}
TCw11	Tpcpul–Tpcpmn	6.04×10^{-12}	5.37×10^{-18}	2.33×10^{-4}	0.066	4.90×10^{-4}
TCw12	Tpcpll–Tpcpln	6.04×10^{-12}	5.37×10^{-18}	2.99×10^{-4}	0.066	4.90×10^{-4}
TCw13	Tpcpv3	2.40×10^{-13}	5.01×10^{-17}	7.05×10^{-5}	0.140	4.90×10^{-4}
PTn21	Tpcpv2–Tpcpv1	2.87×10^{-13}	3.72×10^{-13}	4.84×10^{-5}	0.369	1.10×10^{-1}
PTn22	Tpy	4.61×10^{-13}	3.31×10^{-15}	4.83×10^{-5}	0.234	7.08×10^{-1}
PTn23	Tpbt3	3.00×10^{-12}	1.02×10^{-12}	1.30×10^{-4}	0.353	6.92×10^{-1}
PTn24	Tpp	1.18×10^{-13}	1.05×10^{-13}	6.94×10^{-5}	0.469	4.79×10^{-1}
PTn25	Tpbt2–Tptrv3	2.20×10^{-13}	5.75×10^{-13}	8.32×10^{-5}	0.464	4.79×10^{-1}
TSw31	Tptrv2–Tptrv1	1.00×10^{-12}	2.34×10^{-15}	8.92×10^{-5}	0.042	5.01×10^{-1}
TSw32	Tptrn	7.15×10^{-13}	7.76×10^{-16}	1.29×10^{-4}	0.146	2.88×10^{-5}
TSw33	Tptrl–Tptpul	8.85×10^{-13}	8.71×10^{-17}	1.05×10^{-4}	0.135	7.94×10^{-5}
TSw34	Tptpmn	4.30×10^{-13}	7.94×10^{-18}	1.24×10^{-4}	0.089	1.55×10^{-4}
TSw35	Tptpll	9.02×10^{-13}	2.24×10^{-17}	3.29×10^{-4}	0.115	7.76×10^{-2}
TSw36	Tptpln	1.20×10^{-12}	7.59×10^{-18}	3.99×10^{-4}	0.071	4.79×10^{-5}
TSw37	Tptpv3	1.20×10^{-12}	4.90×10^{-17}	4.92×10^{-4}	0.020	4.90×10^{-4}
CH1vc	Tptpv1/Tptv2/Tpbt1	1.74×10^{-13}	1.58×10^{-12}	7.14×10^{-5}	0.265	4.90×10^{-1}
CH1zc	Tptpv1/Tptv2/Tpbt1	2.50×10^{-14}	2.51×10^{-17}	1.10×10^{-5}	0.193	1.82×10^{-1}

Mean in-situ air permeability (LeCain, 1997; Sonnenthal et al., 1997a,b) assumed to represent the fracture permeability (κ_f). Matrix permeability (κ_m)-model inversions (Bandurraga and Bodvarsson, 1997) based on USGS measurements (Flint, 1998). Fracture porosity (ϕ_f) is calculated from fracture intensity (m/m^2) and calculated hydraulic aperture (Sonnenthal et al., 1997a). Matrix porosity (ϕ_m) is from the USGS (Flint, 1998).

in Table 4, to achieve calibration with observed water saturations and to represent changes in fracture–matrix interaction. For the ECM simulations, these differences have little effect on computed chloride concentrations, because flow and concentrations between fractures and matrix are assumed to be at equilibrium.

A major difference between the 3-D runs using the ECM and the 2-D dual-permeability simulations is the use of a 'fracture–matrix interaction factor' (X_{f-m}) for the dual-permeability simulations (Wu et al., 1998). This factor is applied so as to reduce the effective area for flow between fractures and matrix. The basic premise behind this approach is that only a fraction of the surface area of a fracture may carry water, because of fingering, and that only a fraction of total number of fractures carry the bulk of the fracture flux in the UZ. The factors were derived through model calibration, to matrix saturation and water potential measurements, using an inverse modeling approach and assuming a steady-state system (Wu et al., 1998), and are listed in Table 4. Because of their derivation from inverse modeling the factors are relevant only in terms of the full set of calibrated hydrologic parameters. Thus, their numerical value has no true physical meaning, but they allow for a better match of the model results (which includes conceptual and numerical models) to the measured parameters.

A detailed comparative study of different formulations for the fracture–matrix interaction was presented by Doughty and Bodvarsson (1997). This work utilized a 1-D column from the SSM, corresponding to one of the boreholes, and used similar

hydrologic parameters as those shown in Table 4. This work showed that the travel times for tracer transport increased substantially as the effective area was reduced. However, in the dual permeability model, the fracture spacing is one of the parameters that determines the transport length over which a tracer can equilibrate. Because we have used a mean fracture spacing calculated for fractures 1 m or greater in length (Sonnenthal et al., 1997a), we have necessarily removed a large proportion of possible fractures through which water could potentially flow. The point here is that there are many unknowns, other than the fracture–matrix interaction factor, and the uncertainties are incorporated through the adjustment of many parameters during the inverse calibration procedure.

As will be seen in the model simulations, we are attempting to simulate the distribution of Cl and Sr in a system where the concentrations vary tremendously as a function of space, and somewhat less as a function of time. We are also trying to match concentrations in the simulations to those measured predominantly from matrix porewaters, which are far less sensitive to transient effects than concentrations in fracture waters. Thus, the uncertainties in the fracture–matrix interaction factors are less important for this study, but could be the most important unknown in other systems.

5.3. Boundary conditions, transport parameters, and grids

Boundary conditions at the sides are no mass flux for air, water and chemical components. The top model boundary represents the ground surface of the mountain or, where present, the bottom of the alluvium. The bottom boundary of the model represents the potentiometric surface (water table) and is treated as a Dirichlet boundary (constant, spatially variable gas pressures and a constant liquid saturation). Gas pressure at the bottom boundary is fixed based on an observed pressure value of 0.92 bars at an elevation of 730 m (Ahlers et al., 1995a,b), and an assumption that gravity equilibrium conditions (gas-static) exist in the gas phase. The initial conditions (surface gas pressures) of the system were determined by running TOUGH2 to steady-state using specified bottom gas pressure, specified top and bottom boundary temperatures, and applied surface net infiltration conditions (see Wu et al., this issue).

Water and chemical components are set with a mass flux at the upper boundary. Because of the coarseness of the grid, and the use of first-order upstream weighting for transport, we assume that the hydraulic dispersivity to be zero. The molecular diffusion coefficient for Sr and Cl in aqueous fluids was set to 10^{-10} m^2/s in the matrix and approximately the same value in fractures (the actual value at a given node varies somewhat due to local fracture–matrix connection areas). This value is small enough such that there is little effect at the large scale (between grid blocks); however, diffusion between fracture and matrix can be significant for dual permeability simulations. Nevertheless, dual permeability results would not be better constrained by modifying the diffusion coefficient, or considering dispersion, since the uncertainties in the fracture–matrix interface areas, the fracture spacing, and fracture porosity are much larger. All simulations were performed under isothermal conditions, for two-phase water and air flow. The ECM grid for the LBNL SSM used in the simulations presented in this paper

consists of approximately 39,000 elements. The 3-D ECM submodel has about 18,000 elements. The 2-D dual permeability grid consists of approximately 1900 elements.

5.4. 3-D modeling of chloride transport in the UZ

Four 3-D simulations of chloride transport are presented in this section, of which three simulations used the entire 3-D SSM. These were designed to model the following scenarios.

(1) A steady-state simulation assuming the calculated modern infiltration and precipitation patterns, and the chloride flux based on the mean concentration in precipitation from the Kawich Range (0.55 mg/l).

(2) A steady-state simulation assuming the calculated infiltration and precipitation patterns for a 21 ka glacial maximum event, with the chloride flux also based on the mean concentration in precipitation from the Kawich Range (0.55 mg/l).

(3) A transient case beginning with the steady-state 21 ka chloride and flow solution (conditions at the end of case '2') as the initial conditions, followed by a 10,000 year period with the calculated modern infiltration and chloride flux (conditions at the end of case '1').

(4) A 3-D submodel was constructed from the 3-D SSM corresponding to the recently completed east–west cross-drift (EWCD) (Ritcey et al., 1998). A revised effective chloride concentration in precipitation for the modern climate (0.62 mg/l) was used for comparison to 2-D simulations described below.

In addition, several 2-D dual-permeability simulations are also presented as follows.

(5) A 2-D model was constructed from the 3-D SSM corresponding to the recently completed EWCD (Ritcey et al., 1998). Steady-state and transient simulations were performed (modern climate, glacial maximum, climate change), for the 2-D cross-section using modified hydrologic properties, and a revised effective chloride concentration in precipitation for the modern climate (0.62 mg/l). In addition to a prediction of chloride and strontium concentrations, some objectives of the modeling were to make comparisons of the ECM and dual permeability results, as well as examine differences between the 2-D and 3-D chloride distributions.

5.5. Case 1: 3-D SSM results—modern infiltration

The full 3-D SSM was used to simulate the chloride distribution, assuming the calculated current infiltration pattern and chloride flux. For this simulation, the chloride flux was calculated using the present day precipitation fluxes, with the effective chloride concentration in precipitation set to 0.55 mg/l, the mean value for the Kawich Range (McKinley and Oliver, 1994, 1995; Triay et al., 1996). The surface chloride concentration pattern for this simulation was shown in Fig. 7a. An east–west cross-section through Borehole UZ-14, near the northern part of the repository block, is shown in Fig. 8. The profile shows relatively low chloride concentrations at Yucca Ridge, displaced laterally under Borehole UZ-14. High concentrations underlying valleys do not penetrate as deeply into the system because of the very small infiltration rates. Therefore, lateral

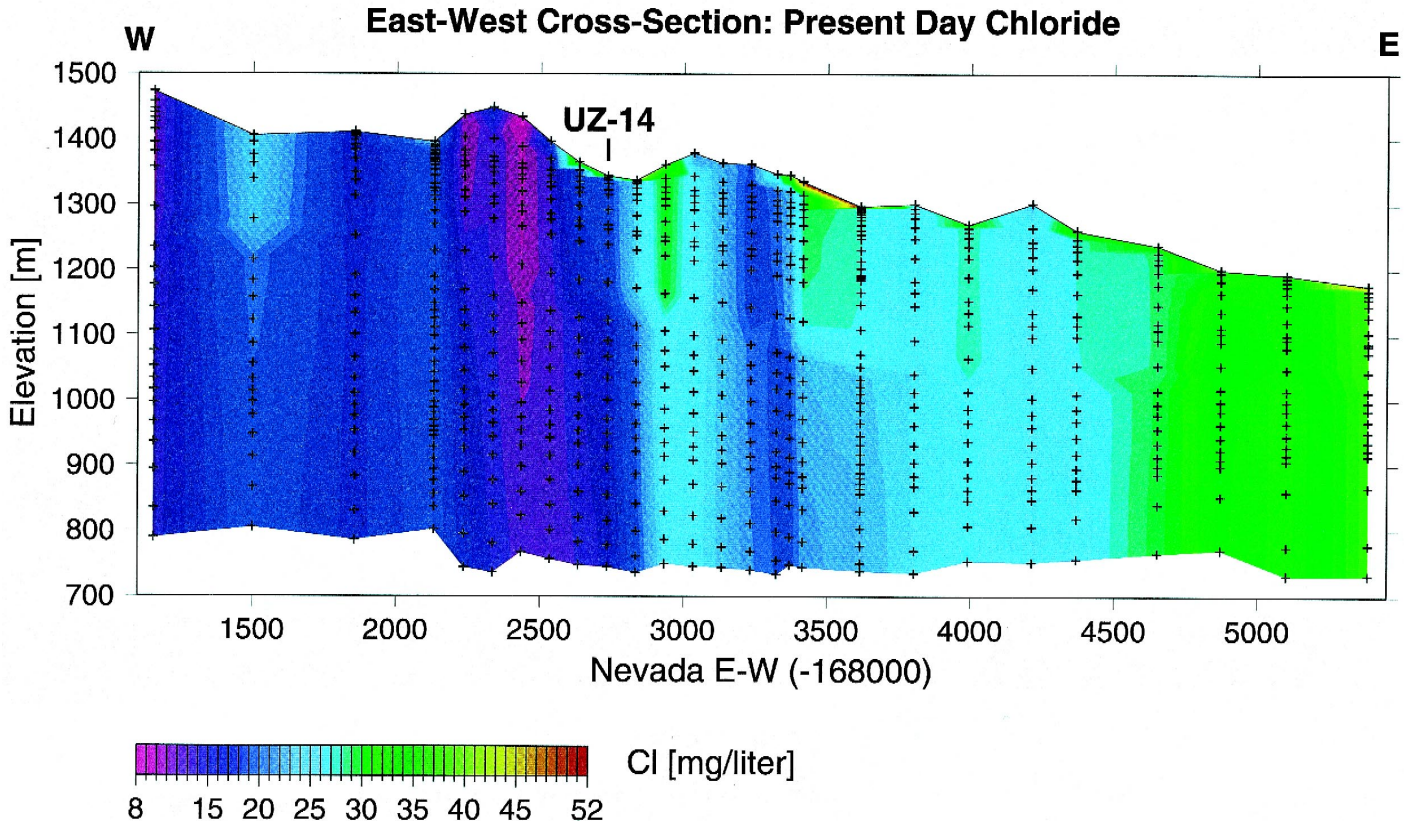

Fig. 8. East–west cross-section, intersecting UZ-14, through the 3-D SSM showing steady-state chloride concentrations for the modern climate. The conditions for this simulation are the present day infiltration and precipitation (Flint et al., 1996), and the chloride concentration of 0.55 mg/l from precipitation (McKinley and Oliver, 1994, 1995; Triay et al., 1996). The thin bedded tuffs in the PTn are demarcated by the region of closely spaced grid nodes, approximately 50 to 100 m below the surface.

flow from high infiltration regions mixes with and nearly eliminates the chloride-rich plumes through dilution. Below the surface, there is very little evaporation, and the chloride concentrations are not affected noticeably.

A north–south cross-section along the entire length of the Main Drift is shown in Fig. 9. The southern half of the ESF shows a pattern of strong lateral flow and dilution of high concentration plumes emanating from alluvium-filled valleys with low concentration waters penetrating from high infiltration regions along Yucca Ridge. Exceptionally high concentrations near the surface at the Ghost Dance Fault are truncated sharply in the PTn by lateral flow.

5.6. Case 2: 3-D SSM results—glacial maximum precipitation

Precipitation last reached a maximum sometime around 21 ka (Flint et al., 1996). Higher levels of precipitation, compared to the modern climate, lasted for at least another 10,000 years, and at 10 ka may have been 50% higher than the modern precipitation rate (Tyler et al., 1996). In this section, steady-state chloride concentrations are simulated for the calculated 21 ka glacial maximum precipitation and infiltration (J. Hevesi, written communication). All numerical methods and rock properties are identical to those used for the previous simulation.

A plan view of the steady-state spatial distribution of chloride at the surface of the model domain is shown in Fig. 7b. Large areas of the model domain in regions of high infiltration have concentrations less than 10 mg/l, consistent with the chloride concentrations in the perched water and SZ. Some of the greatest differences in chloride concentrations between the two climate models are found beneath areas of thick alluvium, where zero infiltration is predicted for the modern climate, but for the 21 ka glacial maximum the minimum infiltration rate is over 1 mm/year. This large change in chloride concentration and its record in the subsurface is supported by the much greater chloride concentrations, seen in the Tiva Canyon tuff, in the North Ramp of the ESF, and at shallower levels in the South Ramp compared to that in the PTn and TSw (Fabryka-Martin et al., 1998).

An east–west cross-section through Borehole UZ-14 for the steady-state simulation is shown in Fig. 10. Concentrations range from about 2 to less than 20 mg/l. Most of the modeled porewater concentrations in the lower part of the TSw and in the CHn are similar to that of the perched water (<10 mg/l). Regions of high chloride and low infiltration near the surface are underlain by low chloride waters, except at the eastern boundary of the model domain, where lateral flow is inhibited.

A north–south cross-section along the Main Drift of the ESF shows the well-defined vertical plumes of higher chloride waters under alluvial channels (Fig. 11). The high concentrations observed in this model (mostly less than 50 mg/l) are significantly lower than concentrations from areas of low infiltration calculated for the modern climate. However, because of the overlap in concentrations from the 21 ka climate and the modern climate, the chloride concentrations in the subsurface are certainly not unique. Waters in the UZ at greater depth having very low chloride concentrations (such as the perched water in SD-7 with a concentration of ~ 4 mg/l) are difficult to reproduce

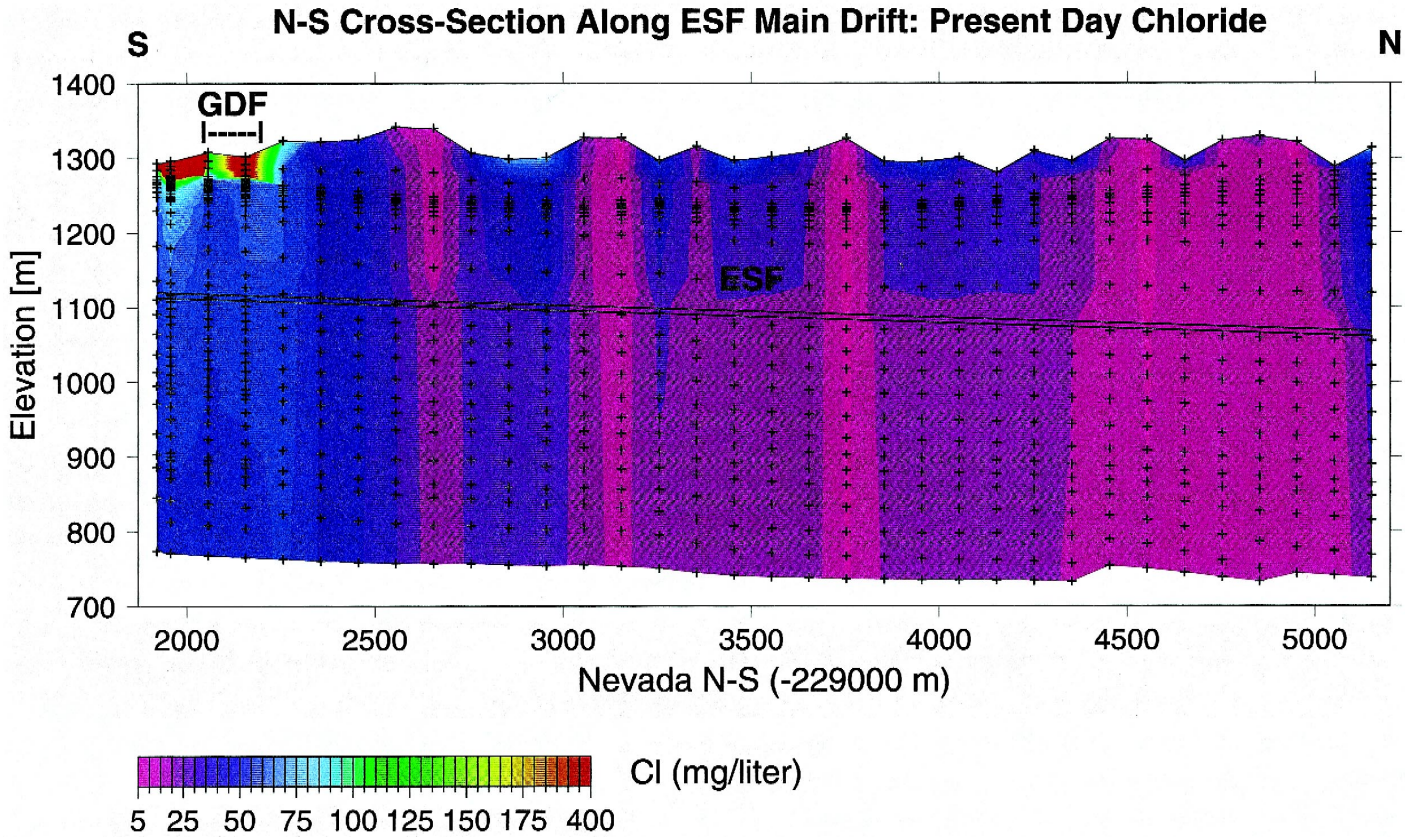

Fig. 9. Steady-state chloride concentrations for the modern climate shown for a north–south cross-section along entire length of the Main Drift in the ESF. "GDF" refers to Ghost Dance Fault.

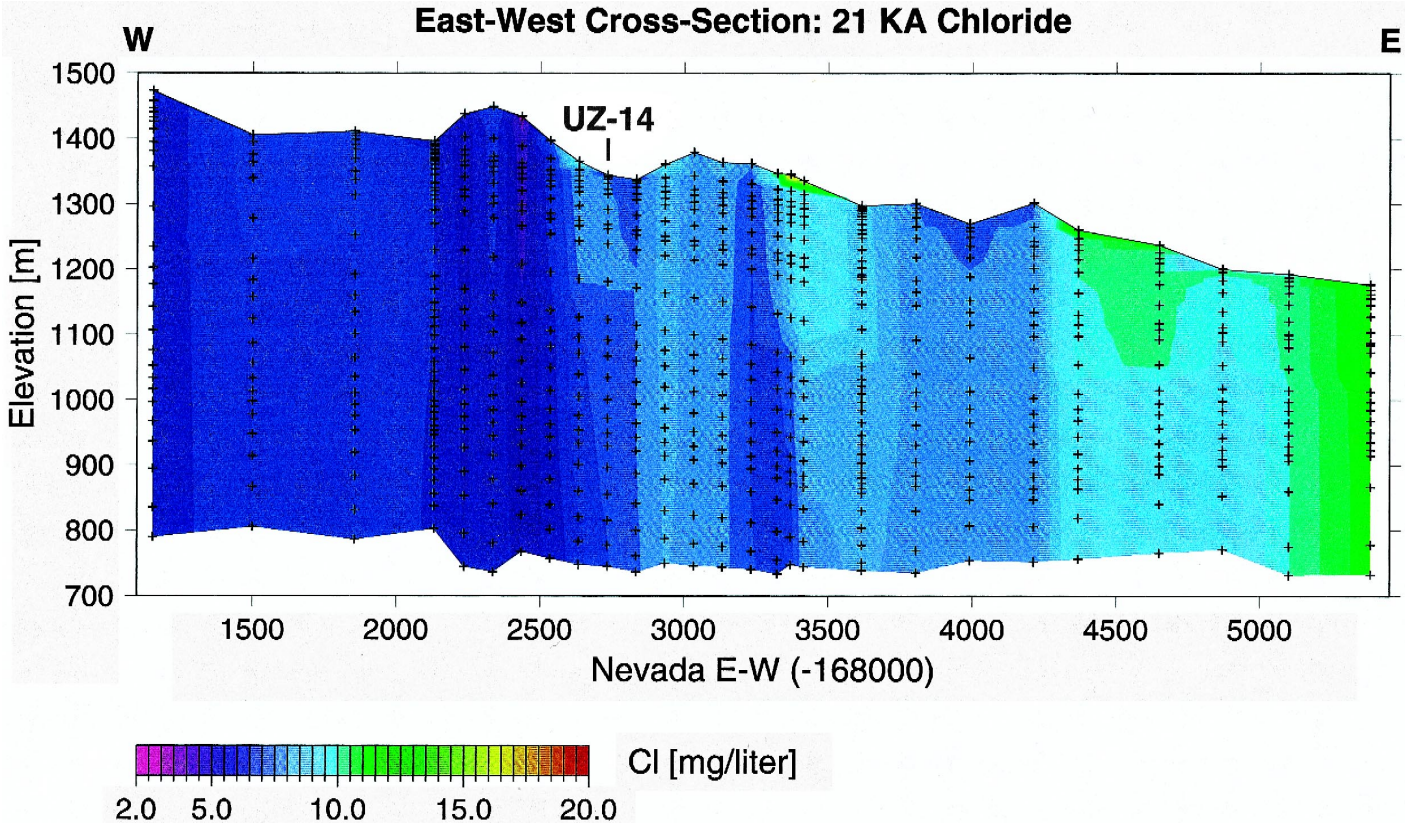

Fig. 10. East–west cross-section showing steady-state chloride concentrations using the 21 ka glacial maximum precipitation and infiltration, and the present day chloride concentration in precipitation. The thin bedded tuffs in the PTn are demarcated by the region of closely spaced grid nodes, approximately 50 to 100 m below the surface.

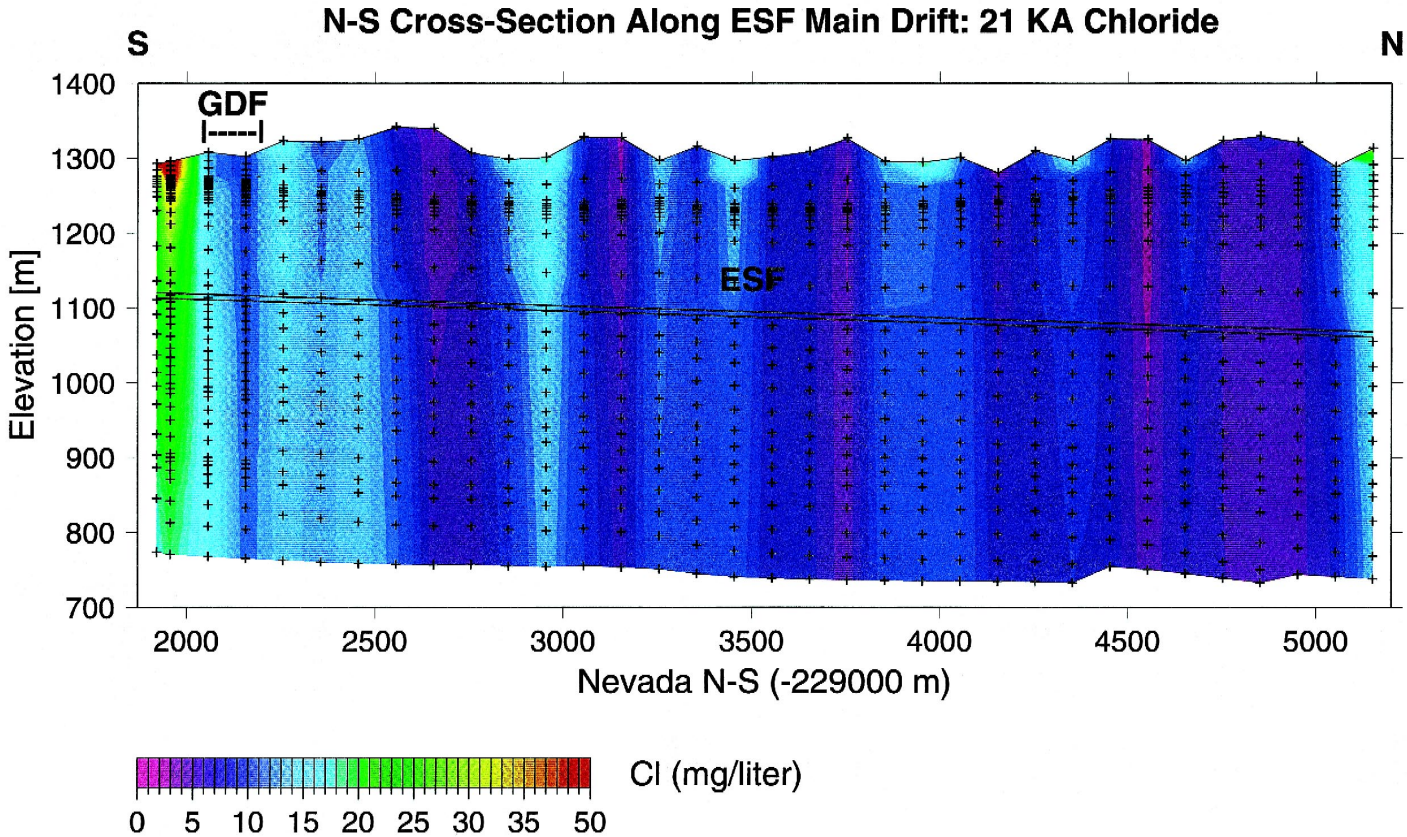

Fig. 11. North–south cross-section along the Main Drift of the ESF, showing steady-state chloride concentrations for the 21 ka glacial maximum climate.

given the low estimated modern infiltration rates. However, a change in the Holocene to a low infiltration rate (~ 1 to 5 mm/year), seems to be necessary to produce the high chloride concentrations in the PTn, parts of the TSw, and the widely varying compositions in the CHn.

5.7. Case 3: 3-D SSM results—transient postglacial change in infiltration and chloride fluxes

The change in climate at approximately 10 ka is a significant dividing line for the hydrologic system at Yucca Mountain. In addition to marking a change in precipitation and infiltration, it is also the time period of interest for the performance of the proposed nuclear waste repository. Therefore, an understanding of the dynamics of the UZ at the period of higher precipitation, and the response of the UZ hydrological system to the past 10,000 years of a more arid climate, is essential to a prediction of the future behavior of the hydrogeologic system and its response to future climate changes.

For this simulation, the present day infiltration and chloride flux was applied for a period of 10,000 years to the steady-state flow and concentration fields calculated from the glacial maximum infiltration. Although, in this simulation, we do not treat the transient effects that can be addressed by a dual permeability formulation, we can get an approximation to larger scale patterns of equilibration and mixing. This is an important first step before running significantly more computation-intensive 3-D dual-permeability transient simulations.

In this transient simulation, surface concentrations have reached their modern values after 10,000 years of the modern infiltration and chloride fluxes. An east–west cross-section through Borehole UZ-14 (Fig. 12) shows the large variation in depths that have been reached by the present day chloride-rich waters. Under ridgetops and side slopes, modern waters have reached the water table, whereas under regions of very low infiltration the front of the chloride-rich plume has just made it into the PTn, leaving much of the underlying Topopah Spring welded tuffs unaffected. Given the assumption of equilibrium between fractures and matrix, this scenario may be an upper limit to the degree of large-scale chemical equilibration expected.

A north–south cross-section along the Main Drift of the ESF (Fig. 13) shows less difference from the modern day concentrations (Fig. 9), except in the Calico Hills unit at the Ghost Dance Fault. Well-developed fingering of younger and older waters in the Calico Hills unit, near the Ghost Dance Fault, was the result of incomplete chemical equilibration between less permeable zeolitic layers and adjacent vitric units, and lateral flow of higher chloride waters from regions of higher percolation fluxes. This layered pattern may help explain the wide variation in chloride concentrations seen in the Calico Hills unit in Borehole UZ-16, which are not so well-developed in boreholes located in regions of higher infiltration.

5.8. Comparison of chloride from 3-D ECM and 2-D dual permeability simulations

Fig. 14 shows the computed chloride concentrations for all simulations plotted as a function of distance in meters from the start of the EWCD at its approximate elevation

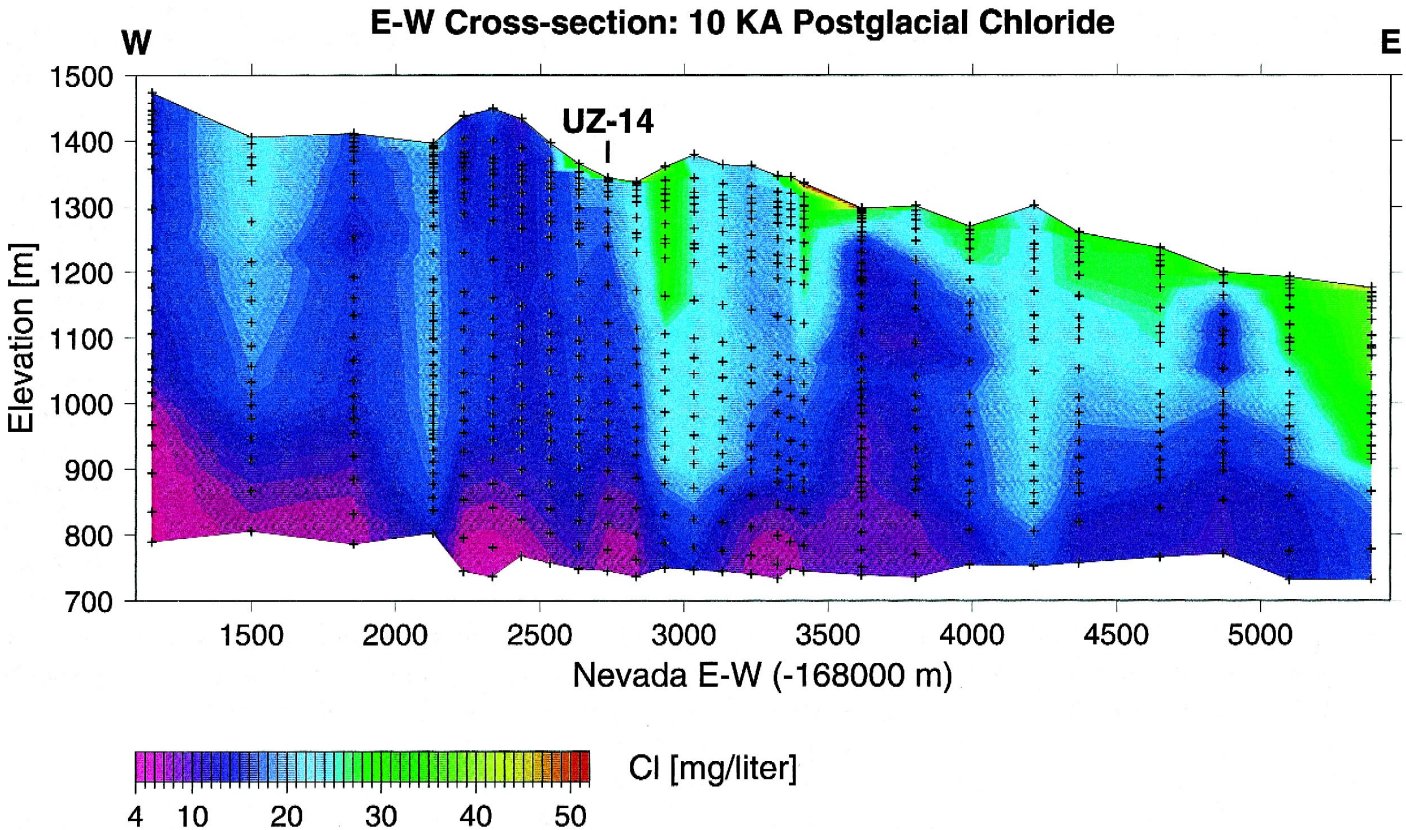

Fig. 12. East–west cross-section showing chloride concentrations, assuming 10,000 years of modern infiltration and chloride flux after a steady-state condition corresponding to the estimated 21 ka glacial maximum precipitation and infiltration. Note regions of 'old' waters beneath alluvial channels at shallow levels near the base of the PTn and below (the PTn is outlined by the closely spaced grid nodes near the surface).

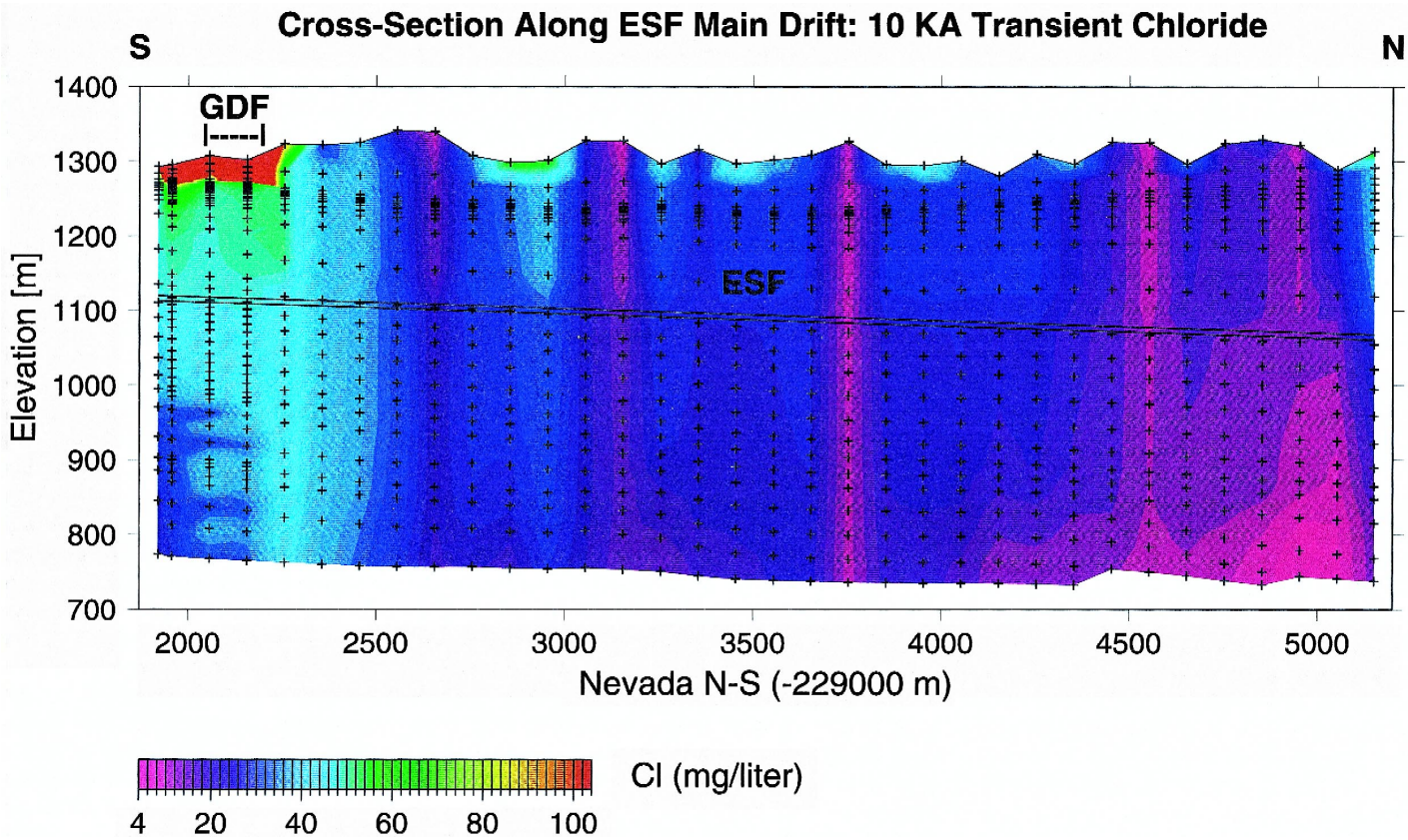

Fig. 13. North–south cross-section showing chloride concentrations, assuming 10,000 years of modern infiltration and chloride flux after the 21 ka glacial maximum precipitation and infiltration.

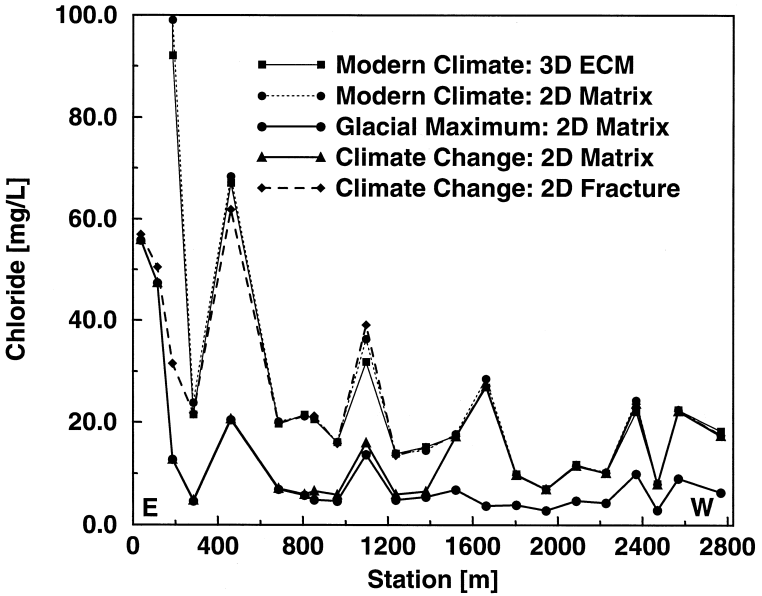

Fig. 14. East–west cross-section comparing chloride concentrations from the 3-D ECM simulations to 2-D dual permeability results, shown plotted as a function of distance from the start of the EWCD (east end is at 0.0 m). Concentrations are taken at the approximate depths of the tunnel.

of 1100 m. The profiles show that for the steady-state modern climate simulations, the ECM and dual permeability runs (matrix chloride (shown) and fracture chloride (not shown)) give nearly identical results, except at the model domain sides which do not receive fluxes from surrounding grid blocks in the 2-D model as in the 3-D model. Fracture and matrix concentrations are also nearly identical for the dual permeability steady-state simulations. Regions of high infiltration (under ridges) are similar to the modern concentrations, because the modern fluid fluxes are sufficient to displace and dilute the Pleistocene waters almost completely. Under regions of lower infiltration, on the west and on the east sides, the depths of penetration of modern waters are substantially less. This shows also that flow to the repository level is generally well predicted by a 2-D model. Below the repository there is considerable lateral flow, mixing effects are more important, and therefore large-scale 3-D models should be employed to model concentration variations.

The climate change simulation shows an interesting break near the center of the profile, where on the west side the matrix concentrations are almost the same as the modern concentrations, but to the east they are close to the glacial maximum concentrations. However, the chloride concentrations in fractures have equilibrated nearly everywhere with the modern values, because of the much higher flow velocities. This behavior illustrates the effect of slow mixing and molecular diffusion between fracture and matrix porewaters. Therefore, actual samples of porewaters taken from matrix blocks may show a range of concentrations, between the modern and climate change values, or between fracture and matrix concentrations.

5.9. Comparison of 3-D site-scale simulation results to borehole measurements

A comparison of the results for different boreholes from 3-D site-scale simulations are used here to assess the infiltration model, chloride fluxes, ages, and degrees of mixing of waters.

Chloride concentrations are plotted in Fig. 15 as a function of elevation from the three SSM simulations, corresponding to the location of Borehole UZ-14. All three simulations generally match the low-concentration perched water and deep porewaters in the Calico Hills and Prow Pass units, yet high concentrations in the PTn and near the top of the Calico Hills and base of the Topopah Spring are well above the model results. Several possibilities exist to explain this discrepancy, including: (1) the calculated infiltration rate may be too high at this borehole even though the mean infiltration rate over the site is approximately correct; (2) the calculated mean infiltration rate is too high, as are some of the individual rates at the boreholes; (3) higher concentration waters at the surface undergo less mixing and retain their concentrations deeper into the section; (4) chloride concentrations in precipitation are higher than estimated.

The possibility of higher chloride concentrations in precipitation was addressed previously and it can be concluded that they could be up to about 30% higher than the

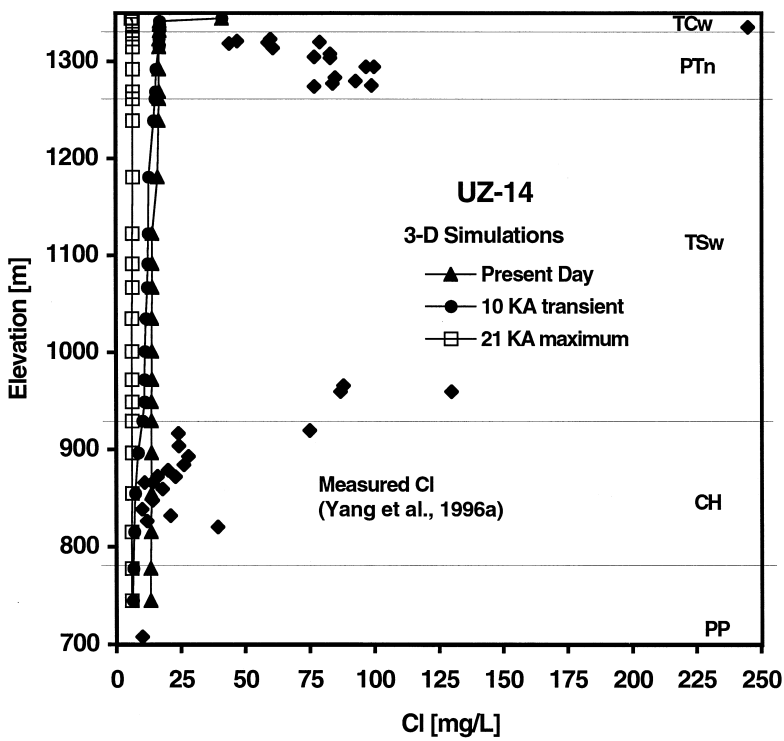

Fig. 15. Borehole concentrations in UZ-14 waters (Yang et al., 1996a), compared to simulations at present day, 21 ka maximum, and 10 ka transient infiltration scenarios.

mean precipitation value of 0.55 mg/l. In Borehole UZ-14, concentrations are about a factor of about five higher in the PTn and about ten higher at the base of the TSw, compared to the values from the model simulation, which cannot be explained by the possible variation in the average chloride initial concentrations. It is unlikely that the mean infiltration is an order-of-magnitude lower; otherwise, the range in concentrations predicted by the model would be significantly greater than observed chloride concentrations. Therefore, local variations in the modern infiltration rate may be predominantly responsible for the large deviations in the model predictions.

In Borehole UZ-16 (Fig. 16), concentrations in the PTn are matched by a mixture of modern chloride-rich water and older chloride-poor waters. This pattern is supported by the profiles observed by Tyler et al. (1996) in thick soil zones at the NTS. Alternatively, the low chloride values in the PTn could be due to more recent flushing of chloride through the column. This may be supported by the presence of high and variable chlorides at depth in the Calico Hills. However, the range of concentrations in the Calico Hills and Prow Pass units is well represented by variable mixing of modern water and water from the 21 ka maximum. Such differences in the borehole profiles are not as pronounced in areas up slope, because large alluvial channels having high chloride concentrations are not present. The highest concentrations predicted by the model are perhaps 50% lower than the maximum concentrations observed, indicating that the infiltration rate is a little lower or the chloride flux a little higher.

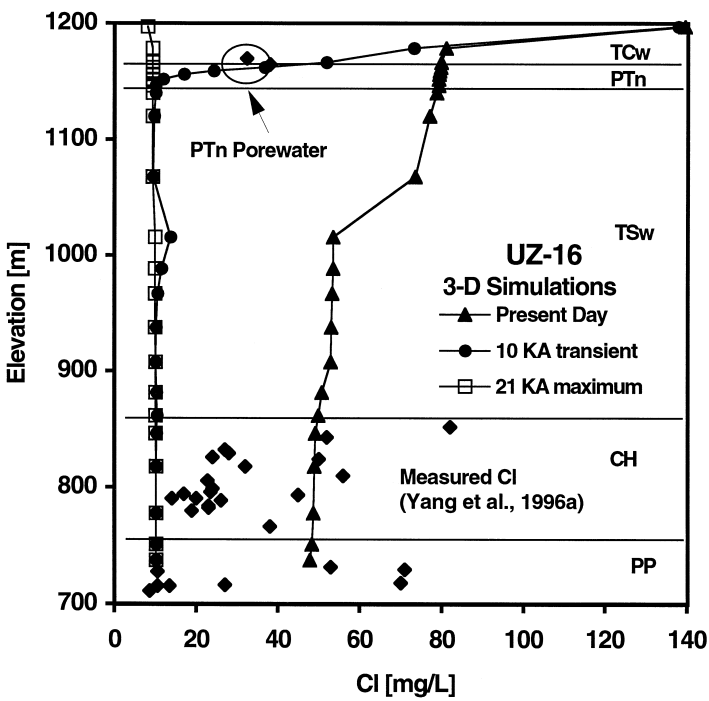

Fig. 16. Borehole concentrations in UZ-16 waters (Yang et al., 1996a), compared to simulations at present day, 21 ka maximum, and 10 ka transient infiltration scenarios.

5.10. Comparison of model results to chloride concentrations in the perched water

Concentrations taken at the level of the perched water in the simulations are compared to the mean values from Yang et al. (1996a) in Table 5. The mean chloride concentration for all perched water bodies is matched best by the 21 ka infiltration and precipitation.

Individually, porewater samples from Boreholes NRG-7a, SD-9, UZ-14, and WT-24 have measured concentrations that are closest to mixtures of the modeled modern and Pleistocene waters, whereas samples from USWG-2 and SD-7 have lower concentrations than the modeled Pleistocene waters. Given that the model predictions of Cl in the PTn are generally underestimated compared to those measured in porewaters from boreholes indicating that the present infiltration rate may be overestimated, the fact that the perched waters have such low concentrations makes it more likely that they contain a large component of Pleistocene age water.

Convincing evidence for the ages of the perched water bodies, based on a good correlation between ^{14}C activities and $^{36}Cl/Cl$ ratios (Robinson et al., 1997), indicate a range of residence times from a few thousand years in Borehole NRG-7A to 8 to 12,000 years in Borehole UZ-14. Although the $^{36}Cl/Cl$ ratio cannot be used to determine an age, a mixing trend should exist between late Pleistocene waters having a ratio of around 1000×10^{-15} and modern waters ($< 10{,}000$ years old) having a ratio of about 500×10^{-15} (Fabryka-Martin et al., 1996). Given that the volume of perched water at Borehole UZ-14 is considerably greater than at NRG-7A, the perched water at UZ-14 may be more representative of the bulk of the perched waters under Yucca Mountain.

5.11. Comparison of 3-D simulation results to porewater chloride in the ESF

Recently, some measurements of chloride in porewaters from samples collected in the ESF have become available (Fabryka-Martin et al., 1998). The first group of samples was collected along the North Ramp of the ESF, mostly in the PTn and in higher porosity samples from the TCw and TSw units. Fig. 17 shows the measured concentra-

Table 5
Cl concentrations (mg/l) at the level of the perched water from 3-D SSM simulations, compared to measured concentrations in perched water from Yang et al. (1996a)

Borehole	Elev. [m]	Modern	10 ka	21 ka	Measured
NRG-7A	821	14.4	6.0	5.5	7.0
SD-9	889	11.1	7.1	5.1	5.6
UZ-14	966	13.8	11.0	6.2	8.6
USWG-2	1020	15.1	13.0	7.3	6.5
SD-7	880	23.0	18.0	9.7	4.1
WT-24	~ 980	17.1	12.9	6.4	8.8
Mean	–	15.8	11.3	6.7	6.8

The chloride concentration for perched water in Borehole WT-24 is from Patterson et al. (1998).

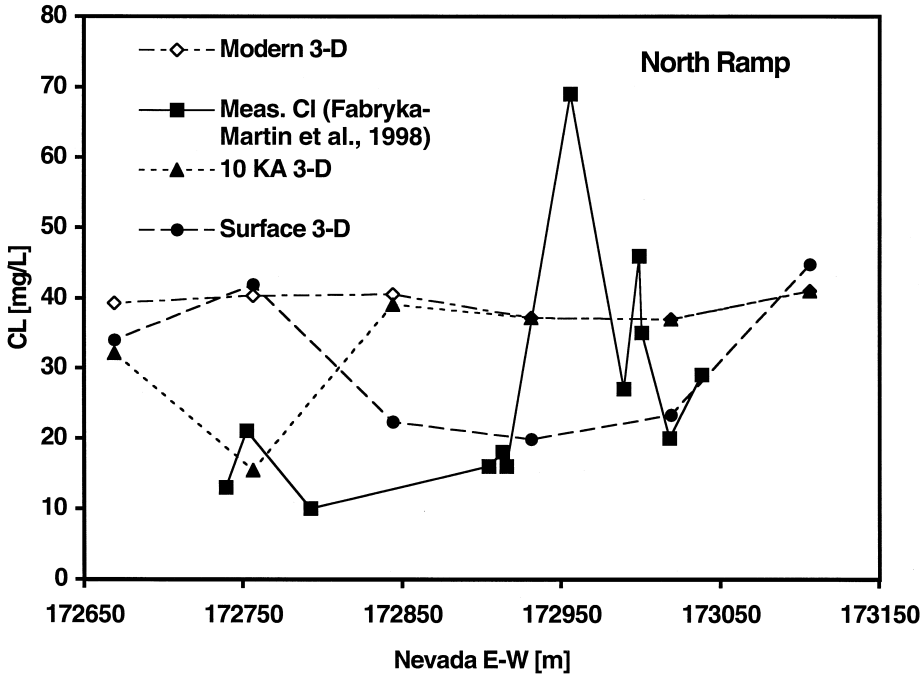

Fig. 17. Chloride concentrations measured in porewaters from the North Ramp of the ESF (Fabryka-Martin et al., 1998) compared to 3-D model results.

tions compared to the model results at approximately the same depth. In the approximately 300 m section where the 12 samples were collected, chloride concentrations range from 10 to 69 mg/l, whereas over a slightly larger section in the model domain, the concentrations in the modern and climate change simulations range from about 15 to 41 mg/l.

Porewater chloride concentrations from the South Ramp of the ESF (Fabryka-Martin et al., 1998) are plotted in Fig. 18, along with values taken from the 3-D SSM simulations. They show a large range in concentrations, from about 17 to 129 mg/l, and in contrast to the North Ramp chloride concentrations, those at the South Ramp are generally higher than the model predictions for the modern climate. The model cannot reflect small-scale variations observed in individual samples, but it does capture the generally greater concentrations seen in the South Ramp, as compared to the North Ramp.

5.12. Modeled strontium concentrations

The 3-D ECM SSM was used to simulate strontium concentrations assuming surface fluxes from precipitation, minimal exchange in unzeolitized rocks (0.02 m^3/kg), and strong exchange in zeolitized tuffs (1.0 m^3/kg; Triay et al., 1996). Surface concentra-

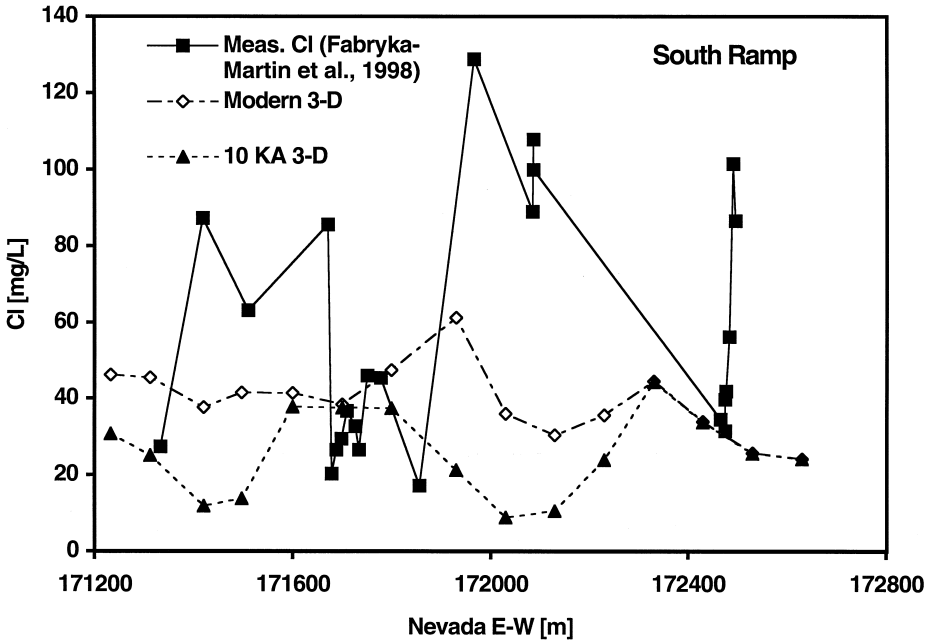

Fig. 18. Chloride concentrations measured in porewaters from the South Ramp of the ESF (Fabryka-Martin et al., 1998) compared to 3-D model results.

tions are shown in Fig. 19, created using the modern infiltration and precipitation, and assuming an effective concentration of 5.8 μg/l in precipitation from Triay et al. (1996). The effective concentration of Sr in precipitation is less constrained than that for chloride, owing to a paucity of measurements.

Strontium concentrations from the 3-D model are plotted in Fig. 20 for an E–W cross-section along the planned cross-drift. They show a similar pattern to the chloride concentrations, except where zeolites are encountered in the CHn and the porewater concentrations drop off precipitously owing to strong ion exchange. The exchange coefficient was not increased in zeolitic rocks along the western margin (Ghost Dance Fault) and therefore there is no reduction in concentrations evident at this location.

Simulated concentration profiles from the 3-D SSM, corresponding to borehole locations, are shown in Fig. 21, along with measured concentrations in perched and porewater samples. The model results show that the porewater strontium concentrations above the zeolites should be in the range of about 0.1 to 0.6 mg/l. The modeled porewater concentrations in the PTn at UZ-4 are similar to the more dilute waters analyzed at UZ-4 and UZ-5, which are encompassed by the same grid block in the SSM. The perched waters at SD-7, NRG-7A, and SD-9 show the very strong effect of exchange with zeolites, that is also well-captured by the model. In contrast, perched waters at UZ-14 and WT-24 are in contact with the unzeolitized basal vitrophyre of the TSw and exhibit much higher Sr concentrations, similar to model predictions of UZ porewaters.

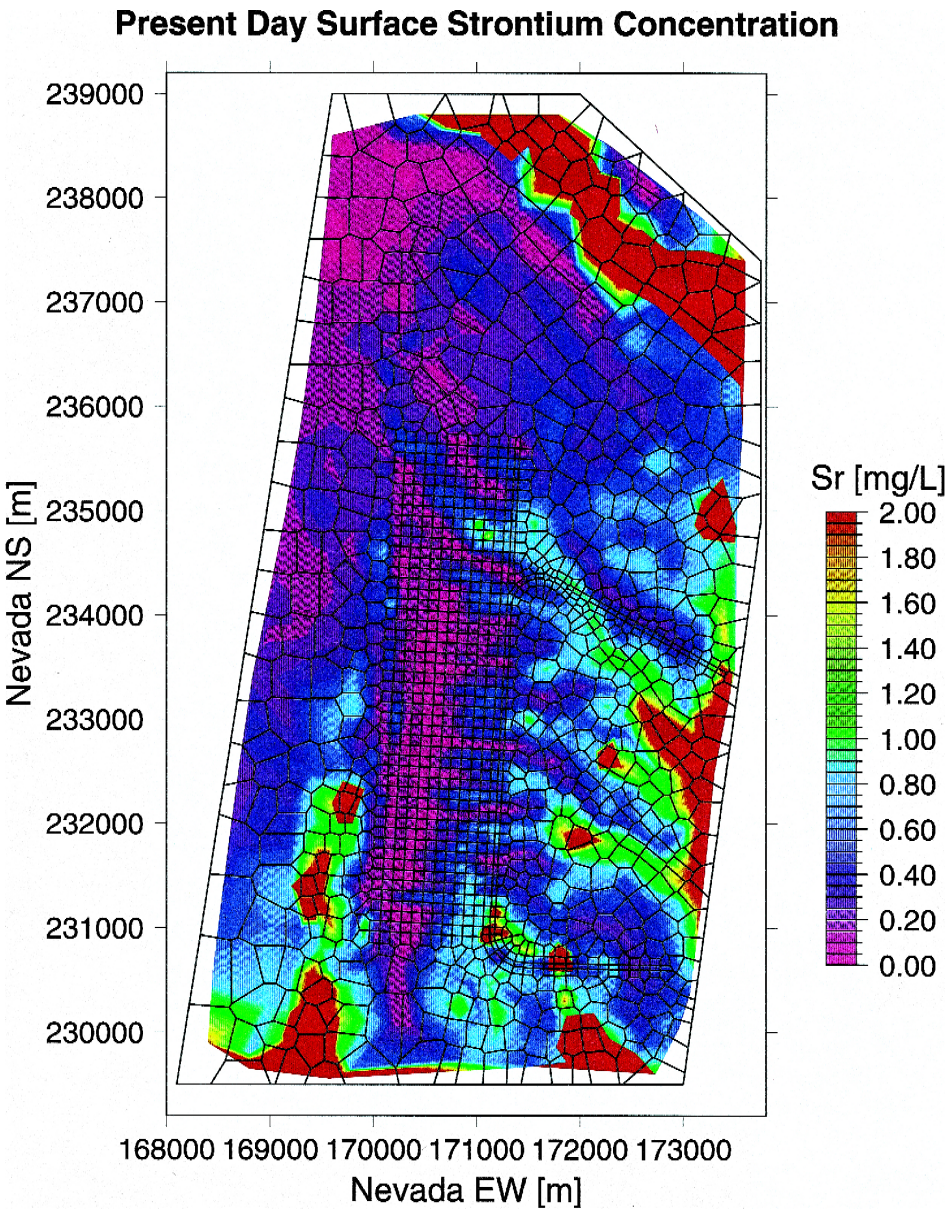

Fig. 19. Steady-state strontium concentrations in the uppermost model layer calculated using the effective concentration precipitation of 5.8 μg/l (Triay et al., 1996) and the spatially variable precipitation and infiltration patterns from Flint et al. (1996).

Some support for a dominantly conservative behavior of Sr in the PTn comes from the covariation of Cl and Sr in UZ-4 and UZ-5 porewaters (Fig. 22; data from Yang et

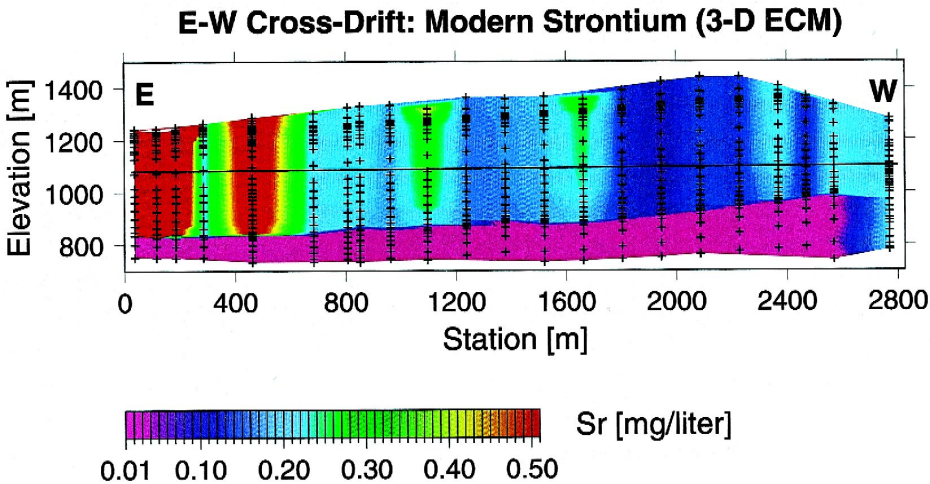

Fig. 20. East–west cross-section showing strontium concentrations from a 3-D ECM simulation, shown plotted in meters along the EWCD (east end is at 0.0 m). Concentrations are taken at the approximate depths of the tunnel.

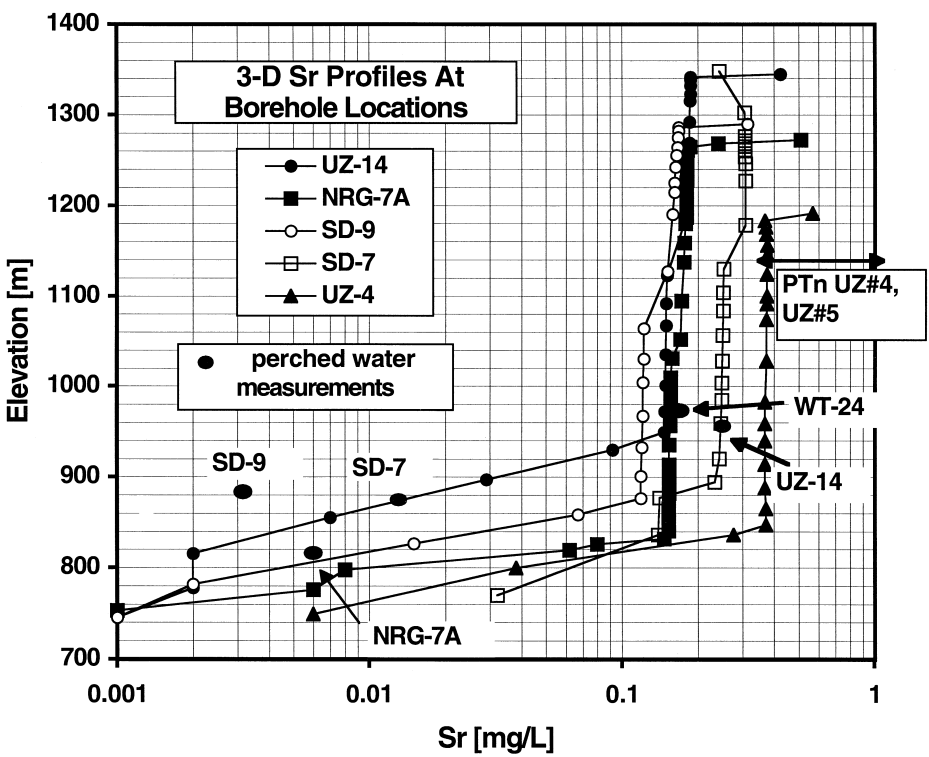

Fig. 21. Sr concentrations from columns in the 3-D model corresponding to locations of boreholes, plotted along with perched waters (Rousseau et al., 1996; Patterson et al., 1998; B. Marshall, personal communication) and porewater analyses (Yang et al., 1988).

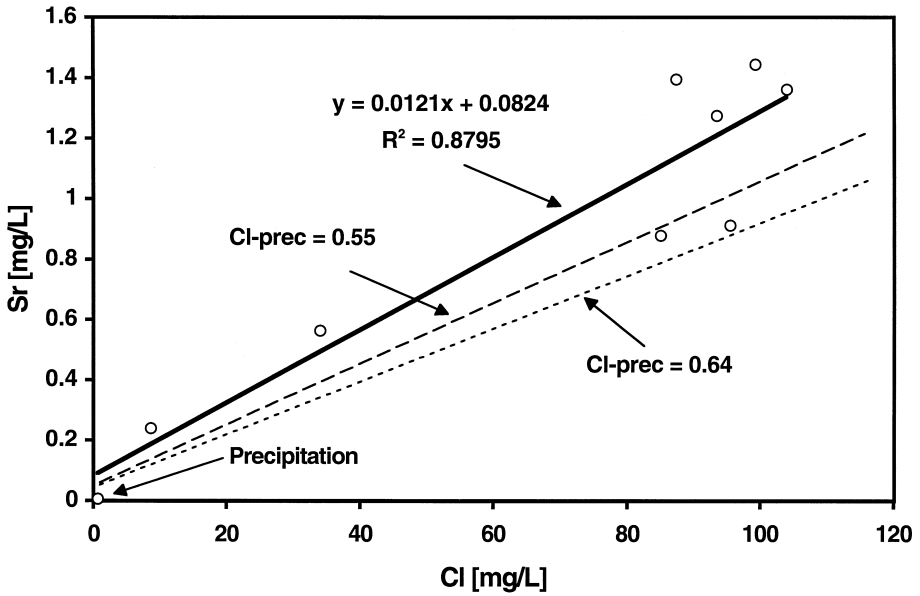

Fig. 22. Sr and Cl concentrations from Boreholes UZ-4 and UZ-5 (Yang et al., 1988), showing best fit line and trends for differing effective Cl concentrations.

al., 1988). The trend is to somewhat higher Sr concentrations than expected for simple evaporation (trends for effective Cl concentrations of 0.55 and 0.64 mg/l are compared), tentatively suggesting a small shift due to water–rock interaction. The Cl/Sr ratios in these samples range from approximately 60 to 105, compared to about 95 for the ratio of the effective concentrations in precipitation given by Triay et al. (1996). The two perched water samples having higher Sr concentrations (UZ-14 and WT-24) have ratios of 25 and 52, respectively (calculated from data of Patterson et al., 1998), indicating somewhat increased Sr concentrations possibly through mineral dissolution, either above or in the basal vitrophyre. This evidence for increased water–rock interaction of perched waters argues against an origin of recent and rapid transport of water to this zone. Elevated $^{234}U/^{238}U$ ratios in these perched waters also points toward greater water–rock interaction (Paces et al., 1998; Patterson et al., 1998).

6. Bounds for the mean infiltration rate

The basic relationship between infiltration rate and chloride concentrations at Yucca Mountain is summarized in Fig. 23 for several possible effective concentrations in precipitation, assuming a calculated mean precipitation rate over the site of 165 mm/year. The range in possible effective concentrations leads to some uncertainty in any model predictions; however given the typically large uncertainties in hydrologic

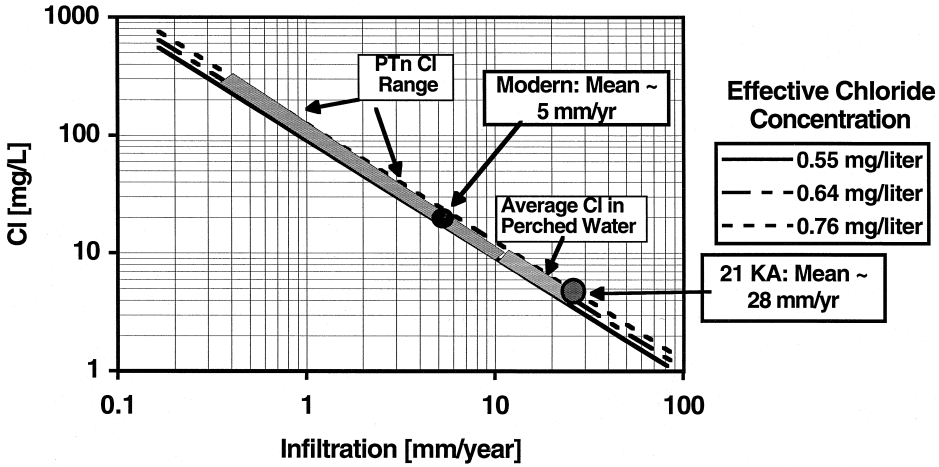

Fig. 23. Calculated mean concentrations (this report) from the current best estimate of mean infiltration and precipitation for the current climate and for the 21 ka glacial maximum (Flint et al., 1996). The range in borehole concentrations for the PTn and the perched water bodies (Yang et al., 1996a,b; Fabryka-Martin et al., 1998) are shown as boxes. The three lines represent possible differences in the estimated concentration of precipitation (precipitation plus windblown dust).

parameters it is quite well constrained. Using the current best estimates of the mean infiltration and precipitation rates at Yucca Mountain (Flint et al., 1996) yields a mean chloride concentration of about 21 mg/l, compared to the approximately 72 mg/l mean chloride (Fabryka-Martin et al., 1998) for the measured borehole concentrations in the PTn. This would suggest that the current mean infiltration rate may be from 1 to 2 mm/year, rather than 4.9 mm/year. However, the recent measurements of concentrations from the ESF have yielded a geometric mean of 26 mg/l (Fabryka-Martin et al., 1998). This is much closer to the mean of 21 mg/l and would result in a mean infiltration of about 4 mm/year (Fabryka-Martin et al., 1998).

The major assumptions in the latter calculations are that the PTn chloride concentrations reflect the modern climatic conditions and that they are representative of the bulk of infiltrating waters, i.e., waters passing through fractures are not a substantial proportion of the total flux and/or readily equilibrate with matrix porewaters. Another aspect, discussed previously, is the stratification observed in PTn porewater concentrations, with the highest concentrations commonly near the top. This may indicate that the higher concentrations in the upper units are actually more representative of the present day climate, and therefore the mean infiltration rate could be less than 4 mm/year.

7. Interpretation of $^{36}Cl/Cl$ ratios

The modeling results for the spatial distribution of chloride have significant implications for the interpretation of measured $^{36}Cl/Cl$ ratios in pore salts collected from the ESF. The relation between measured $^{36}Cl/Cl$ ratios and the chloride contents from extracted pore salts are shown in Fig. 24 (data from Levy et al., 1997). Because the

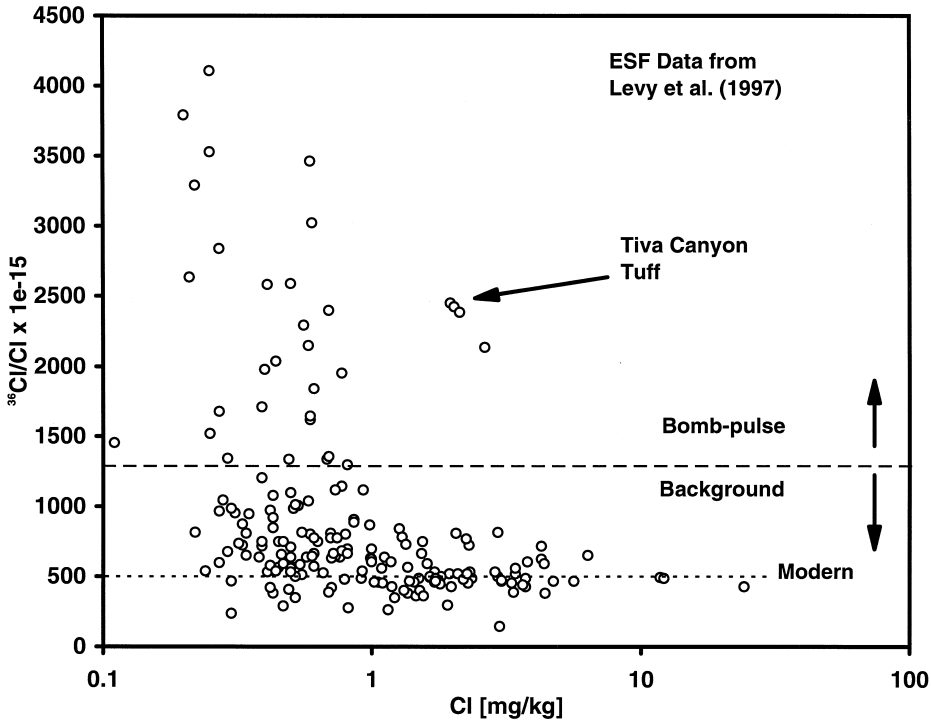

Fig. 24. Measured $^{36}Cl/Cl$ ratios and chloride contents from pore salts in the ESF (Levy et al., 1997).

efficiency of chloride extraction was not the same for all samples (Fabryka-Martin, personal communication) and because of differing water contents this is only an approximate comparison. However, the general trend is that most samples having 'bomb-pulse' $^{36}Cl/Cl$ ratios have low chloride contents. This would suggest that these waters that have traveled rapidly through the UZ in the past 50 years have undergone little evaporation, and little interaction with higher chloride concentration porewaters. A few samples taken from the Tiva Canyon tuff near the entrance of the ESF tunnel are the only bomb-pulse samples having significantly higher chloride contents, suggesting some evaporation has taken place. There are also samples having ratios below the modern day $^{36}Cl/Cl$ ratio of about 500×10^{-15}. These are likely to have been derived from much older waters in which ^{36}Cl has undergone substantial decay or that the pore salts may have been contaminated by rock chloride having a very low $^{36}Cl/Cl$ ratio (Fabryka-Martin et al., 1996).

An example showing the mixing relations for $^{36}Cl/Cl$ as a function of total chloride for infiltrating water carrying a bomb-pulse signature mixing with two end-member pore fluids having a modern ratio is shown in Fig. 25. While evaporation will shift the total chloride concentration at a constant $^{36}Cl/Cl$ ratio, mixing will result in the curves shown. The infiltrating 'bomb-pulse' water is assumed to have a Cl concentration of 1 mg/l and a $^{36}Cl/Cl$ ratio of $10{,}000 \times 10^{-15}$. This water is then mixed with pore fluids having chloride concentrations of 10 and 100 mg/l, both with $^{36}Cl/Cl$ ratios of

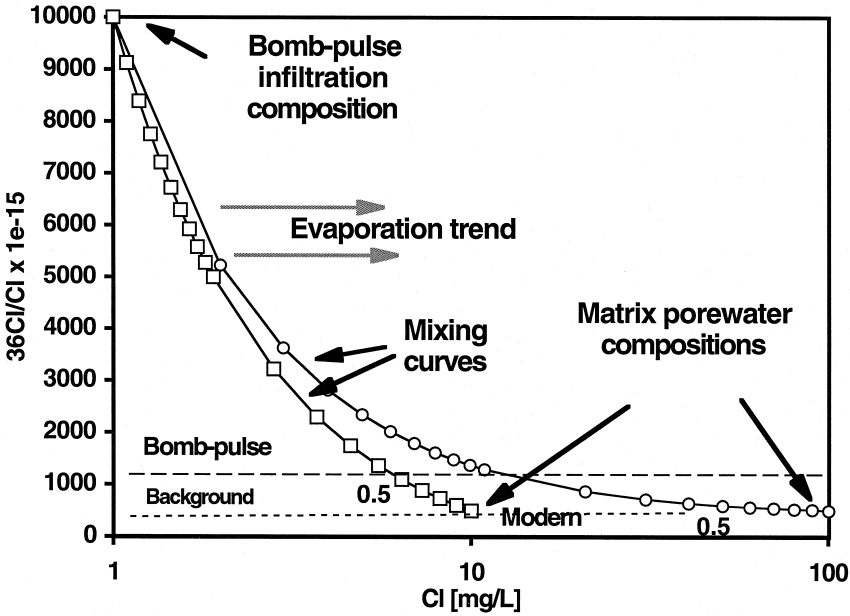

Fig. 25. Hypothetical mixing curves between a 'bomb-pulse' water having a $^{36}Cl/Cl$ ratio of 10,000e−15 and a Cl concentration of 1 mg/l and two possible endmember pore fluids, both having the modern $^{36}Cl/Cl$ ratio of 500e−15. One porewater has a Cl concentration of 10 mg/l and the other 100 mg/l. The $^{36}Cl/Cl$ criterion of 1250e−15 for the bomb-pulse signature is shown as the heavy dashed line (Fabryka-Martin et al., 1996). The evaporation trend is also depicted.

500×10^{-15}. The curves show that a mixture of 50% porewater having 10 mg/l chloride with bomb-pulse water will result in $^{36}Cl/Cl$ ratios just at the ratio that separates a bomb-pulse ratio from a background ratio ($\sim 1250 \times 10^{-15}$, Fabryka-Martin et al., 1996). Mixing the infiltrating bomb-pulse water with porewater having a concentration of 100 mg/l yields a $^{36}Cl/Cl$ ratio indistinguishable from the modern value of 500×10^{-15}. Because the chloride concentration of any particular transient infiltration event will likely be different from the matrix porewaters with which this water mixes, during imbibition we should expect that $^{36}Cl/Cl$ should commonly show this mixing behavior. Comparison of the curves displayed in Fig. 25 to the measured values shown in Fig. 24 seem to suggest that mixing is controlling the general trends of chloride and $^{36}Cl/Cl$ ratios.

Taking into account the relationships outlined above, we may then expect that in areas of high chloride concentrations, at the surface and at depth, the bomb-pulse signal may be strongly masked compared to areas of low chloride and high infiltration. Near the Ghost Dance Fault, high chloride concentrations are predicted by the models and are found in the measured pore salt concentrations, yet bomb-pulse $^{36}Cl/Cl$ ratios were not reported (Levy et al., 1997). The intersection of the ESF and the Ghost Dance Fault was predicted to have bomb-pulse levels of $^{36}Cl/Cl$ (Fairley and Sonnenthal, 1996), based on the presence of a structural feature underlying a likely location for increased runoff

and transient infiltration. The finding of bomb-pulse levels of tritium at the Ghost Dance Fault in the ESF (G. Patterson, personal communication) in locations where the $^{36}Cl/Cl$ ratio is not elevated suggests that bomb-pulse $^{36}Cl/Cl$ ratios may not be evident where matrix porewater chloride concentrations are relatively high.

8. Conclusions

The use of natural tracers such as chloride and strontium can help constrain a wide range of processes in the UZ, such as rates of evapotranspiration, perched water evolution, transient infiltration, and fast-path phenomena. Conceptual models for the spatial and temporal variations in chloride and strontium chemistry at Yucca Mountain were implemented in the 3-D LBNL UZ SSM, and in 2-D dual permeability cross-sections to gain insight into these processes and as another tool to constrain the model parameters and conceptual models of flow and transport. The spatial variation in chloride and strontium concentrations were calculated using maps of precipitation and infiltration rates for the current climate and for the last glacial maximum (about 5.5 times higher mean infiltration rate) and measured concentrations in precipitation and those calculated from estimates of the mean chloride surface fluxes. This study suggests that the current mean infiltration rate ($\sim$ 4.9 mm/year) is probably an upper limit for the site, and depending on the total chloride flux at the surface, the mean infiltration may be as low as 1 to 2 mm/year.

Analysis of the observed chloride concentrations and modeling results suggest that some proportion of Pleistocene age water could be present in the PTn bedded tuffs and in the underlying Topopah Spring welded tuff, predominately under regions of thick alluvium having little infiltration. However, much of the area above the repository does not have thick alluvial cover and is considered to have higher infiltration than areas down slope. Thus, porewaters at the repository level would mostly reflect recharge over the past 10,000 years. The 3-D simulations showed that there is significant mixing in the Calico Hills unit of high-chloride water infiltrating under alluvial channels with low chloride water flowing laterally, resulting in mixed compositions. Perched water compositions are best matched by a mixture of Pleistocene age water with variable amounts of modern water.

In porewaters from the PTn and in some perched waters, Sr concentrations follow a general trend of evaporative concentration of precipitation, similar to chloride but with progressive effects of water–rock interaction. Perched waters that are in contact with zeolitic rocks have much lower Sr concentrations due to strong ion exchange, also indicating that the perched water is poorly mixed or is not a contiguous body of water.

The chloride content of samples collected for $^{36}Cl/Cl$ ratios suggest a mixing trend of low chloride 'bomb-pulse' waters with higher chloride matrix porewaters having a modern $^{36}Cl/Cl$ ratio. This effect is probably responsible for the absence of bomb-pulse $^{36}Cl/Cl$ ratios at locations where elevated tritium concentrations were found and for some of the intermediate $^{36}Cl/Cl$ ratios that could also be attributed to waters having ages greater than 10,000 years.

9. Notation

$C_{i,o}$	Initial concentration of trace element i in the aqueous phase, kg/kg H_2O
C_i	Concentration of trace element i in the aqueous phase, kg/kg H_2O
D	Combined vapor/liquid and solid/liquid distribution coefficient
F	Mass fraction of liquid remaining after evapotranspiration
J_I	Infiltration flux, kg/s
J_P	Precipitation flux, kg/s
J_{Cl}	Chloride flux, kg/s

Acknowledgements

Development of the 3-D site-scale UZ model and the calibrated hydrologic properties, upon which this work was based, was the work of several individuals. In particular, we acknowledge Yu Shu Wu, Charles Haukwa, Mark Bandurraga, Rick Ahlers, Anne Ritcey, and Jennifer Hinds. Discussions with Jerry Fairley, June Fabryka-Martin, and Brian Marshall are appreciated. Reviews by Peter Lichtner, Arend Meijer, John Apps, and Nicolas Spycher are gratefully acknowledged. This work was supported by the Director, Office of Civilian Radioactive Waste Management, US Department of Energy, through Memorandum Purchase Order EA9013MC5X between TRW Environmental Safety Systems and the Ernest Orlando Lawrence Berkeley National Laboratory (Berkeley Lab). The support is provided to Berkeley Lab through the US Department of Energy Contract No. DE-AC03-76SF00098.

References

Ahlers, C.F., Bandurraga, T.M., Bodvarsson, G.S., Chen, G., Finsterle, S., Wu, Y.S., 1995. Performance Analysis of the LBNL/USGS Three-Dimensional Unsaturated-Zone Site-Scale Model. Yucca Mountain Project Level 4 Milestone 3GLM105M. Lawrence Berkeley National Laboratory, Berkeley, CA.

Ahlers, C.F., Bandurraga, T.M., Bodvarsson, G.S., Chen, G., Finsterle, S., Wu, Y.S., 1995. Summary of Model Calibration and Sensitivity Studies Using the LBNL/USGS Three-Dimensional Unsaturated-Zone Site-Scale Model. Yucca Mountain Project Level 4 Milestone 3GLM107M. Lawrence Berkeley National Laboratory, Berkeley, CA.

Altman, S.J., Arnold, B.W., Barnard, R.W., Barr, G.E., Ho, C.K., McKenna, S.A., Eaton, R.R., 1996. Flow calculations for Yucca Mountain groundwater travel time (GWTT-95). SAND96-0819. Sandia National Laboratory, Albuquerque, NM.

Anna, L.O., 1997. Preliminary Three-Dimensional Discrete Fracture Model of the Topopah Spring tuff in the Exploratory Studies Facility, Yucca Mountain Area, Nye County, Nevada. U.S. Geol. Surv. Open File Rep. 97-834, Denver, CO.

Bandurraga, T.M., Bodvarsson, G.S., 1997. Calibrating matrix and fracture properties using inverse modeling. In: Bodvarsson, G.S., Bandurraga, T.M. (Eds.), Development and Calibration of the Three-Dimensional Site-Scale Unsaturated-Zone Model of Yucca Mountain, Nevada. Yucca Mountain Site Characterization Project Milestone. Report LBNL-40376, Chap. 6. Lawrence Berkeley National Laboratory, Berkeley, CA, pp. 191–231.

Bandurraga, T.M., 1996. Geological model development and vertical layering scheme for the numerical grid. In: Bodvarsson, G.S., Bandurraga, M. (Eds.), Development and Calibration of the Three-Dimensional

Site-Scale Unsaturated-Zone Model of Yucca Mountain, Nevada. Yucca Mountain Site Characterization Project Milestone. Report LBNL-39315, Chap. 2. Lawrence Berkeley National Laboratory, Berkeley, CA, pp. 31–61.

Bandurraga, T.M., Wu, Y.S., Ritcey, A.C., Sonnenthal, E., Ahlers, C.F., Haukwa, C., Bodvarsson, G.S., 1997. UZ Site-Scale Model Calibration, FY97. Yucca Mountain Site Characterization Project Milestone SP924UFM4. Lawrence Berkeley National Laboratory, Berkeley, CA.

Bodvarsson, G.S., Shan, C., Htay, A., Ritcey, A., Wu, Y.S., 1997. Estimation of Percolation Flux from Temperature Data. In: Bodvarsson, G.S., Bandurraga, T.M., Wu, Y.S. (Eds.), The Site-Scale Unsaturated-Zone Model of Yucca Mountain, Nevada, for the Viability Assessment. Yucca Mountain Project Level 4 Milestone SP24UFM4, LBNL-40376, Chap. 11, UC-814. Lawrence Berkeley National Laboratory, Berkeley, CA.

Buesch, D.C., Spengler, R.W., Moyer, T.C., Geslin, J.K., 1995. Revised stratigraphic nomenclature and macroscopic identification of lithostratigraphic units of the Paintbrush group exposed at Yucca Mountain, Nevada. U.S. Geol. Surv. Open File Report 94-469. U.S. Geological Survey, Denver, CO.

Dettenger, M.D., 1989. Reconnaissance estimates of natural recharge to desert basins in Nevada, USA, by using chloride-mass balance calculations. J. Hydrol. 106, 55–87.

Doughty, C., Bodvarsson, G.S., 1997. Investigation of conceptual and numerical approaches for evaluating moisture flow and chemical transport. In: Bodvarsson, G.S., Bandurraga, T.M., Wu, Y.S. (Eds.), The Site-Scale Unsaturated-Zone Model of Yucca Mountain, Nevada, for the Viability Assessment. Yucca Mountain Project Level 4 Milestone SP24UFM4; LBNL-40376, Chap. 5. Lawrence Berkeley National Laboratory, Berkeley, CA.

Edwards, A.L., 1972. TRUMP: A Computer Program for Transient and Steady-State Temperature Distributions in Multidimensional Systems. National Technical Information Service, National Bureau of Standards, Springfield, VA.

Fabryka-Martin, J.T., Wightman, S.J., Robinson, B.A., Vestal, E.W., 1994. Infiltration processes at Yucca Mountain inferred from chloride and chlorine-36 distributions. Los Alamos Report LA-CST-TIP-94-O22. Los Alamos National Laboratory, Los Alamos, NM.

Fabryka-Martin, J., Wolfsberg, A.V., Dixon, P.R., Levy, S., Musgrave, J., Turin, H.J., 1996. Summary report of chlorine-36 studies: sampling, analysis and simulation of chlorine-36 in the Exploratory Studies Facility. Los Alamos National Laboratory Milestone Report 3783M. Los Alamos National Laboratory, Los Alamos, NM.

Fabryka-Martin, J.T., Flint, A.L., Sweetkind, D.S., Wolfsberg, A.V., Levy, S.S., Roach, J.L., Woldegabriel, G., Wolfsberg, L.E., 1997. Evaluation of Flow and Transport Models of Yucca Mountain, Based on Chlorine-36 Studies for FY97. Los Alamos Report LA-CST-TIP-97-010, LANL Milestone SP2224M3. Los Alamos National Laboratory, Los Alamos, NM.

Fabryka-Martin, J., Wolfsberg, A.V., Roach, J.L., Winters, S.T., Wolfsberg, L.E., 1998. Using chloride to trace water movement in the unsaturated zone at Yucca Mountain. In: Proceedings of the Eighth International Conference on High-Level Radioactive Waste Management. American Nuclear Society, La Grange Park, IL, pp. 264–267.

Fairley, J., Sonnenthal, E., 1996. Preliminary conceptual model of flow pathways based on Cl-36 and other environmental isotopes. In: Bodvarsson, G.S., Bandurraga, M. (Eds.), Development and Calibration of the Three-Dimensional Site-Scale Unsaturated-Zone Model of Yucca Mountain, Nevada. Yucca Mountain Site Characterization Project Milestone. Report LBNL-39315, Chap. 10. Lawrence Berkeley National Laboratory, Chapter, Berkeley, CA, pp. 380–415.

Faure, G., 1977. Principles of Isotope Geology. Wiley, New York.

Flint, L.E., 1998. Characterization of hydrogeologic units using matrix properties, Yucca Mountain, Nevada. U.S. Geol. Surv. Water Resour. Invest. 97-4243. U.S. Geological Survey, Denver, CO.

Flint, L.E., Flint, A.L., 1990. Preliminary Permeability and Water-retention Data for Nonwelded and Bedded Tuff Samples, Yucca Mountain Area, Nye County, Nevada. U.S. Geol. Surv. Open File Rep. 90-569. U.S. Geological Survey, Denver, CO.

Flint, A.L., Flint, L.E., 1994. Spatial distribution of potential near surface moisture flux at Yucca Mountain. In: Proceedings of the Fifth Annual International Conference on High Level Radioactive Waste Management, Vol. 4. American Nuclear Society, Las Vegas, NV, pp. 2352–2358.

Flint, L.E., Flint, A.L., Hevesi, J.A., 1994. Shallow infiltration processes in arid watersheds at Yucca

Mountain, Nevada. In: Proceedings of the Fifth Annual International Conference High Level Radioactive Waste Management, Vol. 4. American Nuclear Society, Las Vegas, NV, pp. 2315–2322.

Flint, A.L., Hevesi, J.A., Flint, L.E., 1996. Conceptual and Numerical Model of Infiltration for the Yucca Mountain Area, Nevada. Milestone 3GU1623M. U.S. Geol. Surv. Water Res. Invest. Rep. U.S. Geological Survey, Denver, CO.

Geomatrix Consultants, 1997. Unsaturated Zone Flow Model Expert Elicitation Project, Yucca Mountain, NV, GMX No. 3997.

Harrar, J.E., Carley, J.F., Isherwood, W.F., Raber, E., 1990. Report of the committee to review the use of J-13 well water in Nevada nuclear waste storage investigations. UCID-21867. Lawrence Livermore National Laboratory, Livermore, CA.

Haukwa, C., Wu, Y.S., 1997. Grid generation and analysis. In: Bodvarsson, G.S., Bandurraga, T.M., Wu, Y.S., (Eds.), The Site-Scale Unsaturated Zone Model of Yucca Mountain, Nevada, for the Viability Assessment. Yucca Mountain Project Milestone Report SP24UFM4, Chap. 4. Lawrence Berkeley National Laboratory, Berkeley, CA, pp. 1–14.

Hevesi, J.A., Flint, A.L., Istock, J.D., 1992. Precipitation estimation in mountainous terrain using multivariate geostatistics: Part II. Isohyetal maps. Journal of Applied Meteorology 31, 677–688.

Holser, W.T., 1979. Mineralogy of evaporites. In: Burns, R.G. (Ed.), Marine Minerals, Mineralogical Society of America Short Course Notes, Vol. 6. Mineralogical Society of America, Washington, DC, pp. 211–294.

Johnson, T.M., DePaolo, D.J., 1994. Interpretation of isotopic data in groundwater systems: model development and application to Sr isotopic data from Yucca Mountain. Water Resour. Res. 30, 1571–1587.

LeCain, G.D., 1997. Air-injection testing in vertical boreholes in welded and nonwelded tuff, Yucca Mountain, Nevada. U.S. Geol. Surv. Water Resour. Invest. Rep. 96-4262. U.S. Geological Survey, Denver, CO.

Levy, S.S., Sweetkind, D.S., Fabryka-Martin, J.T., Dixon, P.R., Roach, J.L., Wolfsberg, L.E., Elmore, D., Sharma, P., 1997. Investigations of structural controls and mineralogic associations of chlorine-36 fast pathways in the ESF. Yucca Mountain Site Characterization Project Milestone SP2301M4. Los Alamos Report Number LA-EES-1-TIP-97-004. Los Alamos National Laboratory, Los Alamos, NM.

Marshall, B.D., Futa, K., Peterman, Z.E., 1997. Hydrologic Inferences from Strontium Isotopes in Pore Water from the Unsaturated Zone at Yucca Mountain, Nevada, Presented to the American Geophysical Union, Washington DC.

Meijer, A., 1995. Modeling and Experimental Results on Saturated Zone Water Chemistry. LANL Milestone 3387. Los Alamos National Laboratory, Los Alamos, NM.

McKinley, P.W., Oliver, T.A., 1994. Meteorological, Stream-Discharge, and Water Quality Data for Water Year 1992 from Two Basins in Central Nevada. U.S. Geol. Surv. Open File Rep. 93-651. U.S. Geological Survey, Denver, CO.

McKinley, P.W., Oliver, T.A., 1995. Meteorological, Stream-Discharge, and Water Quality Data Water Year 1992 from Two Small Basins in Central Nevada. U.S. Geol. Surv. Open File Rep. 94-456. U.S. Geological Survey, Denver, CO.

Montazer, P., Wilson, W.E., 1984. Conceptual hydrologic model of flow in the unsaturated zone, Yucca Mountain, Nevada. U.S. Geol. Surv. Water Resour. Invest. Rep. 84-4355. U.S. Geological Survey, Denver, CO.

Narasimhan, T.N., Witherspoon, P.A., 1976. An Integrated Finite Difference Method for Analyzing Fluid Flow in Porous Media. Water Resour. Res. 12 (1) 57–64. American Geophysical Union, Washington, DC.

Oldenburg, C.M., Pruess, K., 1995. EOS7R: Radionuclide Transport for TOUGH2. Report 34868. Lawrence Berkeley National Laboratory, Berkeley, CA.

Paces, J.B., Newmark, L.A., Marshall, B.D., Whelan, J.F., Peterman, Z.E., 1996. Ages and origins of subsurface secondary minerals in the Exploratory Studies Facility (ESF). Letter Report, 1996. Milestone Report 3GQH450M. U.S. Geological Survey, Denver, CO.

Paces, J.B., Marshall, B.D., Whelan, J.F., Neymark, L.A., 1997. Geochronology of fracture fill material, ESF and estimated past water fluxes. USGS Level 4 Milestone SPC23FM4. U.S. Geological Survey, Denver, CO.

Paces, J.B., Ludwig, K.R., Peterman, Z.E., Neymark, L.A., 1998. Anomalous groundwater $^{234}U/^{238}U$ beneath Yucca Mountain: evidence of local recharge? In: Proceedings of the Eighth International Conference on High-Level Radioactive Waste Management. American Nuclear Society, La Grange Park, IL, pp. 185–188.

Patterson, G.L., Weeks, E.P., Rousseau, J.P., Oliver, T.A., 1996. Interpretation of Pneumatic and Chemical

Data from the Unsaturated Zone near Yucca Mountain, Nevada. Yucca Mountain Project Report 3GGP605M. U.S. Geological Survey. U.S. Geological Survey, Denver, CO.

Patterson, G.L., Peterman, Z.E., Paces, J.B., 1998. Hydrochemical evidence for the existence of perched water at USW WT-24, Yucca Mountain, Nevada. In: Proceedings of the Eighth International Conference on High-Level Radioactive Waste Management. American Nuclear Society, La Grange Park, IL, pp. 277–278.

Pruess, K., 1991. TOUGH2—A General Purpose Numerical Simulator for Multiphase Fluid and Heat Flow. Report LBL-29400. Lawrence Berkeley National Laboratory, Berkeley, CA.

Pruess, K., Simmons, A., Wu, Y.S., Moridis, G.J., 1996. TOUGH2 software qualification report. Report LBNL-38383. Lawrence Berkeley National Laboratory, Berkeley, CA.

Ritcey, A.C., Wu, Y.S., Sonnenthal, E.L. Haukwa, C., Bodvarsson, G.S., 1998. Final Predictions of Ambient Conditions along the East–West Cross Drift Using the 3-D Site-Scale Model. Yucca Mountain Project Level 4 Milestone SP33ABM4. Lawrence Berkeley National Laboratory, Berkeley, CA.

Robinson, B.A., Wolfsberg, A.V., Viswanathan, H.S., Gable, C.W., Zyvoloski, G.A., Turin, H.J., 1996. Modeling of flow radionuclide migration and environmental isotope distributions at Yucca Mountain. Los Alamos National Laboratory Milestone 3672. Los Alamos National Laboratory, Los Alamos, NM.

Robinson, B.A., Wolfsberg, A.V., Viswanathan, H.S., Bussod, G., Gable, C.W., Meijer, A., 1997. The Site-Scale Unsaturated Zone Transport Model of Yucca Mountain. LANL Milestone SP25BM3. Los Alamos National Laboratory, Los Alamos, NM.

Rousseau, J.P., Kwicklis, E.M., Gillies, D.C. (Eds.), 1996. Hydrogeology of the Unsaturated Zone, North Ramp Area of the Exploratory Studies Facility, Yucca Mountain, Nevada. USGS-WRIR-98-4050 Yucca Mountain Project Milestone 3GUP667M. U.S. Geological Survey, Denver, CO.

Sonnenthal, E.L., Bodvarsson, G.S., 1998. Percolation flux estimates from geochemical and thermal modeling. In: Proceedings of the Eighth International conference on High-Level Radioactive Waste Management. American Nuclear Society, La Grange Park, IL, pp. 130–132.

Sonnenthal, E.L., Ahlers, C.F., Bodvarsson, G.S., 1997a. Fracture and fault properties for the UZ site-scale flow model. In: Bodvarsson, G.S., Bandurraga, T.M., Wu, Y.S. (Eds.), The Site-Scale Unsaturated Zone Model of Yucca Mountain, Nevada, for the Viability Assessment. Lawrence Berkeley National Laboratory Report Number 40376, Chap. 7. Lawrence Berkeley National Laboratory, Berkeley, CA, pp. 1–32.

Sonnenthal, E.L., DePaolo, D.J., Bodvarsson, G.S., 1997b. Modeling the Strontium Geochemistry and Isotopic Ratio in the Unsaturated Zone. In: Bodvarsson, G.S., Bandurraga, T.M., Wu, Y.S. (Eds.), The Site-Scale Unsaturated Zone Model of Yucca Mountain, Nevada, for the Viability Assessment, Chapter 17. Yucca Mountain Project Level 4 Milestone SP24UFM4, Report LBNL-40376, UC-814. Lawrence Berkeley National Laboratory, Berkeley, CA.

Sweetkind, D.S., Barr, D., Polacsek, D., Anna, L., 1997. Integrated Fracture Data in Support of Process Models. Yucca Mountain, Nevada. YMP Report SPG32M3, Administrative Report to the U.S. Department of Energy. U.S. Geological Survey, Denver, CO.

Triay, I.R., Meijer, A., Conca, J.L., Kung, K.S., Rundberg, R.S., Streitelmeier, E.A., 1996. Summary and synthesis report on radionuclide retardation for the Yucca Mountain Site Characterization Project. Milestone 3784M. Los Alamos National Laboratory, Los Alamos, NM.

Tyler, S.W., Chapman, J.B., Conrad, S.H., Hammermeister, D.P., Blout, D.O., Miller, J.J., Sully, M.J., Ginanni, J.M., 1996. Soil-water flux in the Southern Great Basin, United States: temporal and spatial variations over the last 120,000 years. Water Resour. Res. 32 (6), 1481–1499.

Vaniman, D.T., Chipera, S.J., 1996. Paleotransport of lanthanides and strontium recorded in calcite compositions from tuffs at Yucca Mountain, Nevada, USA. Geochimica et Cosmochimica Acta 60, 4417–4433.

Vaniman, D.T., Whelan, J.F., 1994. Inferences of Paleoenvironment from Petrographic, Chemical, and Stable-Isotope Studies of Calcretes and Fracture Calcites. Proceedings of the Fifth International High Level Radioactive Waste Management Conference, Vol. 4. American Nuclear Society, Las Vegas, NV, pp. 2730–2737.

Weeks, E.P., 1997. Major pathways for flow through Yucca Mountain—preliminary thoughts. In: Unsaturated zone flow model expert elicitation workshop, February 3–4, 1997. Amargosa Valley, NV.

Wu, Y.S., Ahlers, C.F., Fraser, P., Simmons, A., Pruess, K., 1996. Software Qualification of Selected TOUGH2 Modules. Report LBNL-39490. Lawrence Berkeley National Laboratory, Berkeley, CA.

Wu, Y.S., Ritcey, A.C., Ahlers, C.F., Hinds, J.J., Mishra, A.K., Haukwa, C., Liu, H.H., Sonnenthal, E.L.,

Bodvarsson, G.S., 1998. 3-D UZ Site-Scale Model for Abstraction in TSPA-VA. Yucca Mountain Project Level 4 Milestone SLX01LB3. Lawrence Berkeley National Laboratory, Berkeley, CA.

Yang, I.C., Turner, A.K., Sayre, T.M., Montazer, P., 1988. Triaxial-compression extraction of pore water from unsaturated tuff, Yucca Mountain, Nevada. U.S. Geol. Surv. Water Resour. Invest. Rep. 88-4189. U.S. Geological Survey, Denver, CO.

Yang, I.C., Rattray, G.W., Yu, P., 1996. Interpretations of chemical and isotopic data from boreholes in the unsaturated-zone at Yucca Mountain, Nevada. Water-Resources Invest. Rep. 96-4058. U.S. Geological Survey, Denver, CO.

Yang, I.C., Yu, P., Rattray, G.W., Thorstenson, D.C., 1996. Hydrochemical Investigations and Geochemical Modeling in Characterizing the Unsaturated Zone at Yucca Mountain, Nevada. U.S. Geological Survey Water Resources Investigation Report. U.S. Geological Survey, Denver, CO.